The Pennsylvania State University
The Graduate School

CONTROL ORIENTED MODELING AND STATE OF HEALTH ESTIMATION FOR LITHIUM ION BATTERIES

A Dissertation in
Department of Mechanical Engineering
by
Githin K. Prasad

Submitted in Partial Fulfillment
of the Requirements
for the Degree of

Doctor of Philosophy

Decemeber 2013

The dissertation of Githin K. Prasad was reviewed and approved* by the following:

Christopher D. Rahn
Professor of Mechanical and Nuclear Engineering
Dissertation Advisor, Chair of Committee

Hosam Fathy
Professor of Mechanical and Nuclear Engineering

Alok Sinha
Professor of Mechanical and Nuclear Engineering

Constantino Lagoa
Professor of Electrical Engineering

Karen A. Thole
Professor of Mechanical and Nuclear Engineering
Head of Department of Mechanical and Nuclear Engineering

*Signatures are on file in the Graduate School.

Abstract

Lithium ion (Li-ion) batteries are attracting significant and growing interest due to their many applications, particularly in hybrid and electric vehicles. Their high energy and high power density render them an excellent option for energy storage in these vehicles. Sophisticated battery management systems (BMS) that ensure long battery life and efficient utilization are based on low order electrochemical models that can accurately capture the battery dynamics. This thesis develops reduced order, linear models of Li-ion batteries that can be used for model-based power train simulation, design, estimation, and control in hybrid and electric vehicles. First, a reduced order model is derived from the fundamental governing electrochemical charge and Li^+ conservation equations, linearized at the operating state of charge and low current density. The equations are solved using analytical and numerical techniques to produce the transcendental impedance or transfer function from input current to output voltage. This model is then reduced to a low order state space model using a system identification technique based on least squares optimization. Given the prescribed current, the model predicts voltage and other variables such as electrolyte and electrode surface concentration distributions. A second model is developed by neglecting electrolyte diffusion and modeling each electrode with a single active material particle. The transcendental particle transfer functions are discretized using a Padé Approximation. The explicit form of the single particle model impedance can be realized by an equivalent circuit with resistances and capacitances related to the cell parameters. Both models are then tuned to match experimental EIS and pulse current-voltage data.

As Li-ion cells age, they experience power and energy fade associated with impedance rise and capacity loss, respectively. Identification of key aging parameters in lithium ion battery models can validate degradation hypotheses and provide a foundation for State of Health (SOH) estimation. This thesis develops and simplifies an electrochemical model that depends on three key aging parameters, cell

resistance, solid phase diffusion time and the capacity factor. Off-line linear least squares processing of voltage and current data from fresh and aged NCM and LFP cells produce estimates of these aging parameters. An adaptive gradient based recursive estimator is also designed that can estimate these aging parameters on-board a vehicle in real time. The estimated parameters vary monotonically with age, consistent with accepted degradation mechanisms such as solid electrolyte interface (SEI) layer growth and contact loss.

Finally, a control oriented degradation model is developed for LFP cells by incorporating the aging mechanism of SEI layer growth in the negative electrode with a nonlinear single particle model. This is the major degradation mechanism in LFP cells because the positive electrode does not appreciably age due to its extreme stability. The model predicts the experimentally measured capacity loss and increase in film resistance.

Table of Contents

List of Figures viii

List of Tables x

Acknowledgments xi

Chapter 1
Introduction 1
1.1 Research Contributions and Motivation 1
1.1.1 Research Contribution 1
1.1.2 Research Motivation 1
1.2 Background 4
1.2.1 Battery Models 4
1.2.2 Degradation Mechanisms 5
1.2.3 Aging Models 6
1.2.4 State of Health Estimation 7
1.3 Overview of the dissertation 8

Chapter 2
Impedance Model Development 10
2.1 Introduction 10
2.2 Working of a Lithium Ion Battery 10
2.3 Governing Equations 11
2.3.1 Conservation of Species 13
2.3.2 Conservation of Charge 14
2.3.3 Reaction Kinetics 15
2.3.4 Cell Voltage 16

2.4 Impedance model formulation 16
2.4.1 Linearization 16
2.4.2 Impedance Solution 18
2.4.3 FEM Electrolyte Diffusion 22
2.4.4 Overall System Transfer Function 24
2.5 Single Particle Model 24
2.6 Capacity Modeling 25

Chapter 3
Model Discretization **27**
3.1 Introduction 27
3.2 Pole/Residue Realization 27
3.3 Padé Approximation 32
3.4 First Principles Equivalent Circuit Model 37
3.5 Experimental Validation 38

Chapter 4
State of Health Estimation **42**
4.1 Introduction 42
4.2 Least Squares Parameter Estimation Algorithm 45
4.2.1 Experimental Data for NCM and LFP cells 47
4.2.2 State of Health Estimation for NCM and LFP cells 49
4.3 Recursive Parameter Estimation 54
4.3.1 Recursive Parameter Identification from Experimental Data for fresh NCM cells 55

Chapter 5
Development of a Control Oriented Degradation Model for a Lithium Iron Phosphate Battery **58**
5.1 Introduction 58
5.2 Model Development 59
5.3 Calibration and Validation of the Degradation Model 63

Chapter 6
Conclusions and Future Work **68**
6.1 Conclusions 68
6.2 Future Work 69
6.2.1 Development of Better Aging Models and Validation 69
6.2.2 Identification of Minimally Degrading Current Profiles . . . 70
6.2.3 Inclusion of the Effect of Temperature 70

Bibliography **71**

List of Figures

1.1 Electrified vehicles (a) Hyundai Sonata Hybrid (b) Chevrolet Volt (c) Nissan Leaf. 3

2.1 Lithium-Ion Cell Model. 12

3.1 Frequency Response: Transcendental transfer function (black) vs Reduced order model (red). 30
3.2 Electrolyte Concentration Distribution, $c_e(x,t)$, Time Response: 5C discharge from 60% SOC at various times 31
3.3 Solid Phase Surface Concentration Distribution, $c_{s,e}(x,t)$, Time Response: 5C discharge from 60% SOC at various times 32
3.4 Current Density Distribution, $j(x,t)$, Time Response: 5C discharge from 60% SOC at various times. 33
3.5 Frequency response: full order SP model (Blue) vs padé approximated SP model (red). 35
3.6 Equivalent circuit of a padé approximated single particle model. . . 38
3.7 Impedance frequency response: transcendental transfer function (green-dotted), reduced order model (blue dash-dotted), padé approximated single particle model (red dashed), and experimental EIS (green-dotted). 40
3.8 Experimental (black-solid),single particle model (red-dashed) and reduced order model(blue-dashed) pulse charge/discharge time response. 41

4.1 Impedance frequency response: SP model(blue-solid)and SP model with only positive electrode(red-dashed). 43
4.2 Open Circuit Potential of an LFP electrode. 44
4.3 Experimentally measured capacity versus age for NCM cells 48
4.4 Experimentally measured capacity versus age for LFP cells 49

4.5 NCM - Pulse Charge/Discharge Response: (a) Input current and (b) Measured voltage (black-solid) and fitted model response (red-dashed) . . . 51
4.6 LFP - Pulse Charge/Discharge Response: (a) Input current and (b) Measured voltage (black-solid) and fitted model response (red-dashed) 52
4.7 Estimated Resistance ($\hat{R}_T, +$), diffusion time (τ_D^+, o), and capacity factor ($\mathcal{C}^+, \bullet$) versus age for NCM cells. . . . 53
4.8 Estimated Resistance ($\hat{R}_T, +$), diffusion time (τ_D^-, o), and capacity factor ($\mathcal{C}^-, \bullet$) versus age for LFP cells. . . . 54
4.9 Recursive parameter estimator block diagram . . . 56
4.10 Gradient based recursive parameter estimation for a fresh NCM cell:(a) Current, (b) Voltage, (c) Error, (d) Normalized parameter estimates (Resistance (blue), Diffusion rate (Red)) . . . 57

5.1 Discharge Response at 0.1C: Measured voltage (black-solid) and model response (red-dashed) . . . 64
5.2 Measured capacity (black-solid) and model predicted capacity (red-dashed) . . . 65
5.3 Estimated Resistance Increase (black-solid) and model predicted film resistance increase (red-dashed) . . . 66

List of Tables

3.1 Coefficient values 36
3.2 Circuit parameters in terms of cell parameters 38
3.3 Parameters for Li-Ion Cell Model. 39

5.1 Parameters for the LFP Cell Aging Model. 67

Acknowledgments

First and foremost, I thank my Lord Jesus Christ for this excellent learning experience and helping me successfully complete my doctoral studies here at Penn State. I would like to express my deepest and heartfelt gratitude to my advisor Dr. Christopher Rahn for providing me with the wonderful opportunity to work with him. His astute and timely guidance was extremely helpful through out my PhD. Moreover, he taught me the patience and optimism to handle the hurdles faced during research.

I would also like to extend my sincere gratitude towards my committee members, Dr. Hosam Fathy, Dr. Alok Sinha, and Dr. Constantino Lagoa for their invaluable feedback. I would also like to thank Dr. Yancheng Zhang for providing me with the experimental data and his insightful tips.

I am extremely grateful to my parents Prasad Koshy and Laly Prasad, and my wife Jyothi K. Baby for their unconditional love and support. Their continued faith in me and constant motivation helped me overcome all my academic and non academic challenges during my graduate life.

Finally, I would like to thank all my labmates and friends for all their help and support.

I dedicate this work to my Lord Jesus Christ, parents and wife.

"Most of the important things in the world have been accomplished by people who have kept on trying when there seemed to be no hope at all."– Dale Carnegie

Chapter 1

Introduction

1.1 Research Contributions and Motivation

1.1.1 Research Contribution

This dissertation presents contributions in the area of modeling and estimation of lithium ion batteries, with focus on their application in battery management systems of hybrid and electric vehicles. The highlights of this dissertation are as follows:

1. Development of low order physics based battery models that can be easily implemented on battery management systems.

2. Design of Off-line and On-line State of Health Estimators by identifying aging parameters using a least squares approach and gradient update method respectively.

3. Development of a control oriented degradation model for a lithium iron phosphate cell by incorporating the aging mechanism of SEI layer growth on the negative electrode particle

1.1.2 Research Motivation

Hybrid and electric vehicles have tremendous potential to reduce greenhouse gases in the atmosphere and the dependance on non renewables such as gasoline and

diesel fuel. By 2020 it is estimated that more than half of the new vehicle sales will mostly consist of hybrid-electric, plug-in hybrid, and all-electric models [1]. Lithium ion (Li-ion) batteries play a key role in this huge shift. High energy and power density of Li-ion batteries render them a better option for energy storage than nickel metal hydride batteries in these vehicles. Li-ion batteries also have a longer cycle life, low self-discharge rate and no memory effects.

A class of Li-ion batteries, the lithium iron phosphate (LFP) batteries (in which the positive electrode is made up of $LiFePO_4$) compared to cells with other positive electrode chemistries such as $LiCoO_2$ (LCO) and $LiNi_{1/3}Co_{1/3}Mn_{1/3}O_2$ (NCM) are growing considerably particularly in their application of electric and hybrid vehicles. Their low cost and highly safe nature make them an excellent choice of energy and power for these type of vehicles. Moreover the material is available in plenty and less toxic compared to cobalt, manganese or nickel. Padhi *et al* [2] introduced and studied the olivine structured $LiFePO_4$ (LFP) material for the positive electrode in which the insertion/extraction proceeds via two phase process. The ordered olivine crystalline structure renders the material extremely stable and safe under high thermal and other abuse conditions [3]. MacNeil *et al*[4] studied and compared the thermal stability of seven different cathode using differential scanning calorimetry and ranked LFP material as the safest amongst all.

Figure 1.1 shows three vehicles that employs Li-ion batteries as a source of energy. Hyundai Sonata hybrid in Fig 1.1a is a hybrid electric vehicle (HEV) which combines a 2.4-liter engine with six-speed automatic transmission, and a 30kW electric motor and lightweight lithium polymer batteries to produce a full gasoline-electric hybrid with 37 miles per US gallon in the city and 40 miles per US gallon on the highway (b) Chevrolet Volt is a plug-in hybrid (PHEVs) in which the battery pack charges directly from the electric grid and runs the vehicle for a distance in pure electric mode with zero gas consumption and emissions. The 2011 Chevrolet Volt has a 16 kWh / 45 Ah lithium-ion battery pack that can be charged by plugging the car into a 120-240 V AC residential electrical outlet using the provided charging cord. The vehicle also has an internal combustion engine that can be used to extend the electric-only range or increase the speed above the electric-only limit. After the batteries have been depleted to a specified level,

Figure 1.1. Electrified vehicles (a) Hyundai Sonata Hybrid (b) Chevrolet Volt (c) Nissan Leaf.

the vehicle operates in full hybrid mode until it can be fully recharged from the grid. (c) Nissan leaf is an all electric vehicle(EV) that uses an 80 kW and 280 Nm front-mounted synchronous electric motor driving the wheels, powered by a 24 kWh lithium ion battery pack rated to deliver up to 90 kilowatts power.

However, today's electric and hybrid electric vehicles employ an excess number of batteries due to the overconservative charge and discharge limits designed by the battery manufacturers to prevent premature battery degradation and hence maintain a longer battery life. This substantially increases the total weight and cost of the vehicle which are major obstacles in the widespread recognition and adoption of electric vehicles. Bulk of this problem can be solved by the use of a sophisticated battery management system which can efficiently utilize the batteries and maintain long life. In general, the battery system is composed of the battery pack and the battery management system (BMS). The BMS performs important functions such as controlling the charge and discharge by setting current and voltage limits and hence protecting the battery from overcharging. The BMS also provides accurate estimates of the State of Charge (SOC) and State of Health (SOH), balances the cells in the pack and protects them from thermal runaway. Such an advanced battery management system are based on electrochemical models that can accurately capture the internal battery dynamics and hence assist in the efficient utilization of batteries.

1.2 Background

1.2.1 Battery Models

The Li-ion electrochemical system is non-linear and infinite dimensional complicating the development of an accurate model. Modeling of Li-ion batteries has followed two main approaches: Equivalent circuit models and models based on the fundamental principles of physics and electrochemistry. Equivalent circuit models [5, 6, 7, 8, 9, 10, 11, 12, 13, 14, 15, 16] are the most widely developed and studied models due to their low order and easy integration with the BMS electronics. Equivalent circuit models which consists of resistances and capacitances do not retain any links with the underlying physicochemical processes in the cells. Generally they are lumped models with less parameters. Often, these models are empirical and cannot be used for integrated design of the battery pack and BMS.

On the other hand, fundamental models capture the essential battery dynamics and have a much better prediction capability compared to empirical / equivalent circuit models [17, 18, 19, 20] but their complexity can be a significant barrier to BMS design. First principle electrochemical models using porous electrode and concentrated solution theories were developed in [17, 18] to study the internal dynamics of a Li-ion battery. The governing partial differential equations are numerically solved in a computational fluid dynamics framework, making this approach computationally expensive and too slow for real time applications. Ramadass *et al.* [21] incorporate capacity fade in the model. An extensive review of the existing mathematical models for both Li-ion and Nickel battery systems is provided by Gomadam *et al* [22]. In a typical HEV or Plug in HEV, batteries are usually pulse charged and discharged within a relatively narrow state of charge(SOC) range from 30% to 70%. A reduced order model that has been linearized at 50% SOC, for example, can be sufficiently accurate and low order for model-based BMS.

However, modeling of lithium iron phosphate batteries (LFP) cells is an extremely complex issue and still an open research topic with discrepancies and contentions associated with the lithiation intercalation kinetics in the LFP electrode. Malik *et al* [23] have done an extensive study in identifying and understanding the kinetic mechanisms that are responsible for rapid charging and discharging in LFP electrodes. They studied the LFP electrode kinetics at three different length

scales - bulk, single particle and the multi-particle scale. Srinivasan and Newmann [24] developed a physics based model that accounts for the distinct phases in the lithiated and delithiated forms of the LFP electrode. A shrinking core approach was used to model the phase change in which a core of one phase is covered with a shell of the second phase with transport of Li-ions in the shell driving the movement of the phase boundary. Several researchers have also done excellent work on developing simple physics based mathematical models for LFP cells based on a single particle approach [25, 26, 27]. From a controls perspective, Marcicki *et al* [28] developed an improved Padé approximated single particle model by including the concentration and potential dynamics of the electrolyte phase.

1.2.2 Degradation Mechanisms

Aging in Li-ion batteries which leads to its capacity and power fade is a very serious and challenging issue. Battery degradation is an extremely complex process and difficult to understand since it occurs from a number of reactions and interactions in the electrodes and electrolyte. Capacity and power fade occur due to variety of reasons such as growth of a passivation layer on the positive/negative electrodes, decomposition of the electrolyte, melting and corrosion of the current collectors etc. Diagnosis of aging can be done by both electrochemical techniques such as galvanostatic cycling, hybrid pulse power characterization(HPPC),electrochemical impedance spectroscopy and physical analysis techniques like X-ray diffraction, Raman spectroscopy, scanning electron microscopy(SEM) and transmission electron microscopy (TEM)[29]. Researchers have extensively studied and reviewed the various aging mechanisms in both the negative and positive electrodes [30, 31, 32, 33].

In the negative electrode, the reaction of the electrolyte with the electrode at the interface is the major cause of aging. The electrolyte undergoes reductive decomposition and irreversible consumption of lithium ions takes place at the electrode / electrolyte interface. The products form a protective solid electrolyte interface (SEI) layer around the electrode. The SEI film consists of two layers, a thin inner layer made of inorganic compounds and a thicker porous outer layer composed of organic products [34]. The amount of irreversible charge capacity that is consumed during the formation of the SEI was found to be dependent on the specific surface

area of the graphite. On a long time scale, the SEI penetrates into pores of the electrode and in addition may also penetrate into the pores of the separator. This may result in a decrease of the accessible active surface area of the electrode. The increase in electrode impedance is considered to be caused by the growth of the SEI as well as by changes of the SEI in composition and morphology. Moreover, contact loss (mechanical or electronic) within the composite electrode results in higher cell impedance, and thus, has to be considered as another major cause for aging. One inevitable source for contact loss is the volume changes of the active anode material, which may lead to mechanical disintegration within the composite electrode. Contact loss (i) between carbon particles, (ii) between current collector and carbon, (iii) between binder and carbon, and (iv) between binder and current collector can be the result. Also, the electrode porosity, which is a key feature for good anode performance, since it allows the electrolyte to penetrate into the bulk of the electrode, is certainly affected by the volume changes of the active material.

In lithium metal oxide cathodes (positive electrode), the capacity fading mechanisms are still not understood completely and hence are still of increasing research interest. In general number of changes on the positive electrode such as degradation of components like conducting agents, binder, corrosion of current collector, oxidation of electrolyte and interfacial film formation are responsible for battery aging. These effects do not occur separately and are influenced by cycling conditions. According to Vettel *et al* [30] charge capacity fading of positive electrode material are caused by structural changes during cycling, chemical decomposition/dissolution reaction and surface film modification.

1.2.3 Aging Models

From the perspective of battery management systems, it is extremely important to develop models that can capture the aging dynamics accurately. This could enable better prediction of battery state of health(SOH)and hence assist in the development of control algorithms that can optimize the use of batteries by minimizing degradation. However, modeling of battery aging is extremely complex and a clear understanding of aging mechanisms is necessary to study life performance of batteries. The SEI layer formation on the negative electrode is the most com-

mon and studied mechanism which is responsible for a capacity loss in batteries by their consumption of active lithium ions. Physics based degradation models have been developed by incorporating the SEI layer growth [21, 35, 36]. Randall *et al* [37] reduced the complexity of the aging model developed by Ramadass *et al* [21] using a simple incremental approach. Aging models have also been developed for cells with LFP positive electrode chemistry using the SEI layer growth mechanism since the positive electrode does not undergo any degradation owing to its stable olivine structure [38].

1.2.4 State of Health Estimation

State of health in a lithium ion battery is typically defined as the ratio of the current capacity over the nominal capacity of a fresh battery and monotonically decreases as the battery ages. Impedance also rises as a battery ages, decreasing the maximum power output and efficiency. Researchers have extensively studied the capacity and power fade in Li-ion batteries [39, 40, 41]. Power fade is primarily due to an increase in internal resistance or impedance. Internal resistance causes ohmic losses that waste energy, produce heat, and accelerate aging. Li-ion batteries lose capacity over time due to degradation of the positive and negative electrodes and the electrolyte. The degradation mechanisms are complex, coupled, and dependant on cell chemistry, design, and manufacturer [30].

As mentioned before, considerable effort has been put into the development of high fidelity battery models that accurately predict voltage given the input current and model parameters [17, 19]. The model parameters that provide the best match between the model predicted and experimentally measured voltage change with age. The change in system parameters due to aging depends on the degradation mechanism in a given cell. If the predominant degradation mechanism can be determined then the parameters that are most closely associated with that mechanism would be most likely to change. If the degradation mechanism involves unmodeled dynamics in the cell, however, then the correlation between the mechanism and system parameters becomes unclear.

Ramadass *et al.* [41] link cell aging to the change of only a few parameters in an electrochemical battery model. For a Li-Ion cell, they find that the solid elec-

trolyte film resistance and the solid state diffusion coefficient of the anodic active material are linked to cell degradation. Schmidt *et al.* [42] found that electrolyte conductivity and cathodic porosity are key parameters to estimate the rate capability fade and the capacity loss of a Li-Ion cell. Zhang *et al* [43] characterized the cycle life of lithium ion batteries with $LiNiO_2$ cathode and their study revealed that the impedance rise and capacity fade during cycling are primarily caused by the positive electrode. An SEI layer forms on the positive electrode and it thickens and changes properties during cycling, causing cell impedance rise and power fade.

Parameter estimation techniques based on equivalent circuit models have been developed to quantify the degradation in Li-ion battery. Remmlinger *et al.* [44] monitor the state of health of Li-ion batteries in electric vehicles using an on-board internal resistance estimation technique. Kalman filters [45, 46, 5, 6, 7] have been developed to estimate the state of health using the equivalent circuit models. Troltzsch *et al.* [47] characterize aging effects in Li-ion batteries using impedance spectroscopy. Kim *et al*[48] implement a dual sliding mode observer to estimate the capacity fade in lithium ion batteries.

1.3 Overview of the dissertation

Chapter 2 presents the development of an transcendental impedance transfer function for a Li-ion battery from the fundamental governing electrochemical charge and Li^+ conservation equations that are linearized at the operating state of charge and low current density. The equations are solved using analytical and numerical techniques to produce the transcendental impedance or transfer function from input current to output voltage. A similar approach is used to develop an impedance transfer function for a single particle model, by neglecting electrolyte diffusion and modeling each electrode with a single active material particle.

Chapters 3 presents discretization methods to reduce the order of the transcendental transfer functions developed in Chapter 2. The transcendental impedance transfer function is then reduced to a low order state space model using a system identification technique based on least squares optimization. Given the prescribed current, the model predicts voltage and other variables such as electrolyte and electrode surface concentration distributions. The transcendental particle transfer

functions for the single particle model are discretized using a Padé Approximation. The explicit form of the single particle model impedance can be realized by an equivalent circuit with resistances and capacitances related to the cell parameters. Both models are then tuned to match experimental EIS and pulse current-voltage data.

Chapter 4 presents techniques to estimate SOH by tracking parameters that vary as the battery degrades. An offline as well as an online parameter identification algorithm is presented. The offline method employs a linear least squares technique to estimate the battery parameters whereas the online estimation technique uses a recursive technique based on gradient update. The estimated parameters can be correlated to the mechanisms responsible for the battery degradation. The aging parameters are estimated for both NCM and LFP cells.

Chapter 5 presents the development of a control oriented degradation model for an LFP cell using SEI layer growth mechanism as the major factor responsible for capacity fade. The model is calibrated and predicts experimental capacity loss and resistance increase.

Chapter 6 presents the conclusions and future work.

Chapter 2

Impedance Model Development

2.1 Introduction

This chapter presents the development of impedance models from the fundamental governing electrochemical charge and Li^+ conservation equations that are linearized at the operating state of charge and low current density. The governing equations are solved using analytical and numerical techniques to produce a transcendental impedance transfer function. Later, the chapter presents the development of a single particle model under the assumption of a single electrode particle and negligible electrolyte diffusion.

2.2 Working of a Lithium Ion Battery

Figure 2.1 shows a schematic diagram of the Li-Ion cell model. The 1D domain from the negative current collector ($x = 0$) to the positive current collector ($x = L$) consists of three domains: the negative composite electrode (width = δ_-), separator (width = δ_{sep}), and positive composite electrode (width = δ_+). Lithium metal oxide ($LiMO_2$) and lithiated carbon (Li_xC) are the active materials in the positive and negative electrodes, respectively. The metal in the positive electrode is a transition metal, typically Co. The active materials are bonded to metal foil current collectors at both ends of the cell and electrically insulated by a microporous polymer separator film or gel-polymer. Liquid or gel-polymer electrolytes enable

lithium ions (Li^+) to diffuse between the positive and negative electrodes. The lithium ions insert into or deinsert from the active materials via an intercalation process. During discharge the Li^+ ions diffuse to the surface of the negative electrode spherical particle where it reacts and transfers into the electrolyte. These positive ions migrate through the electrolyte to the positive electrode and reacts with the positive electrode particle at the surface and diffuses into the inner regions. The insulating separator forces electrons to follow an opposite path through an external circuit or load. The binder and filler in these composite electrodes improve the electron transport across the solid phase.

In the positive electrode during charge, the active material is oxidized and lithium ions are de-intercalated as follows

$$\mathrm{Li_{1-x}CoO_2 + xLi^+ + xe^- \overset{\text{discharge}}{\underset{\text{charge}}{\rightleftarrows}} LiCoO_2}. \tag{2.1}$$

In the negative electrode during charge, the active material is reduced and lithium ions that migrate from the positive electrode travel through the electrolyte via diffusion and ionic conduction and are intercalated as follows

$$\mathrm{Li_xC \overset{\text{discharge}}{\underset{\text{charge}}{\rightleftarrows}} C + xLi^+ + xe^-}. \tag{2.2}$$

Reactions (2.1) and (2.2) reverse for discharge.

2.3 Governing Equations

Four partial differential equations govern the dynamics of Li-Ion batteries: Conservation of species and charge in the electrode and electrolyte. These equations are coupled by the Butler-Volmer equation. The model presented here is often termed a pseudo-2D model because one dimension is x and the other is the radial dimension in the spherical particles r. The particles are assumed to be distributed throughout the electrodes and modeled as a particles embedded in the electrode at each value of x. Thus, at each x there is also a radial coordinate r corresponding to the particle embedded at that point. It is called a *pseudo*-2D model because the neighboring particles are not directly coupled unlike most 2D PDEs. The em-

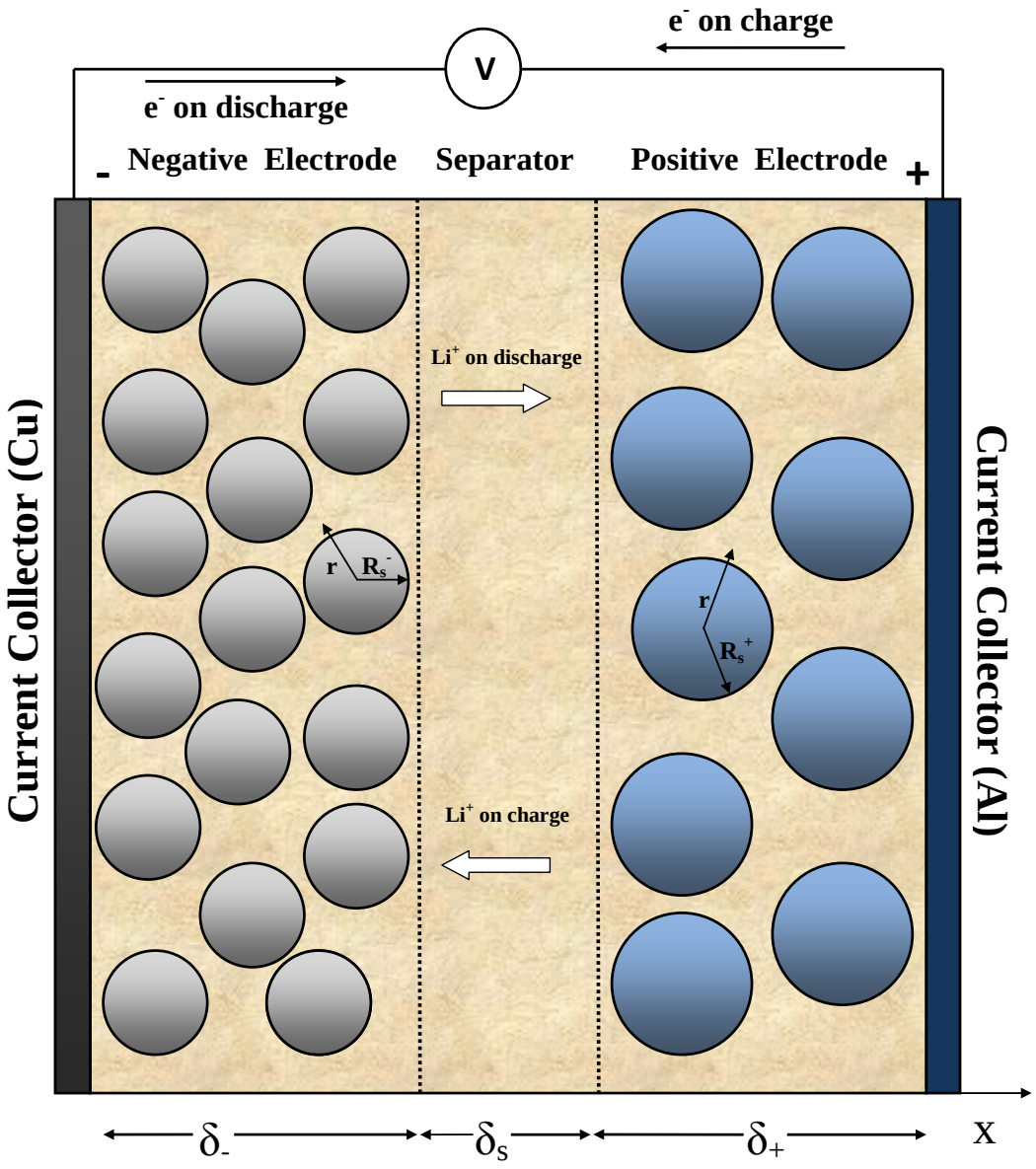

Figure 2.1. Lithium-Ion Cell Model.

bedded particles couple to the electrode through the r direction and the electrode is coupled through the x direction but there is no direct path for ions to flow from inside one particle to an adjacent particle.

2.3.1 Conservation of Species

The composite electrodes are modeled using porous electrode theory, meaning that the solid phase electrode particles are assumed to be uniformly distributed throughout the electrolyte phase. Conservation of Li^+ in a single spherical active material particle is described by Ficks law of diffusion,

$$\frac{\partial c_s}{\partial t} = \frac{D_s}{r^2}\frac{\partial}{\partial r}\left(r^2\frac{\partial c_s}{\partial r}\right) \quad \text{for } r \in (0, R_s), \tag{2.3}$$

where $r \in (0, R_s)$ is the radial coordinate, $c_s(r,t)$ is the concentration of Li ions in the particle as a function of radial position and time, and D_s is the solid phase diffusion coefficient. We use the subscripts s, e, and s,e to indicate solid phase, electrolyte phase, and solid/electrolyte interface, respectively. The boundary conditions are

$$\left.\frac{\partial c_s}{\partial r}\right|_{r=0} = 0, \tag{2.4}$$

$$D_s \left.\frac{\partial c_s}{\partial r}\right|_{r=R_s} = -\frac{j}{a_s F}, \tag{2.5}$$

where $j(x,t)$ is the rate of electrochemical reaction at the particle surface (with $j > 0$ indicating ion discharge), F is Faraday's constant (96487 C/mol), and a_s the specific interfacial surface area. For the spherical active material particles occupying electrode volume fraction ε_s, $a_s = 3\varepsilon_s/R_s$. Equations (2.3) - (2.5) are applied on a continuum basis across each electrode giving solid phase concentration a 2D spatial dependency, *i.e.* $c_s(x,r,t)$. The electrochemical model depends only upon concentration at the particle surface, $c_{s,e}(x,t) = c_s(x,R_s,t)$.

Conservation of Li^+ in the electrolyte phase yields

$$\varepsilon_e \frac{\partial c_e}{\partial t} = D_e^{eff}\frac{\partial^2 c_e}{\partial x^2} + \frac{\left(1-t_+^o\right)}{F} j \quad \text{for } x \in (0, L), \tag{2.6}$$

where $c_e(x,t)$ is the electrolyte phase Li concentration, ε_e is the electrolyte phase

volume fraction, t_+^o is the transference number of Li^+ with respect to the velocity of solvent. The effective diffusion coefficient is calculated from a reference coefficient using the Bruggeman relation $D_e^{eff} = D_e \varepsilon_e^p$ that accounts for the tortuous path that Li+ ions follow through the porous media. We assume that ε_e, t_+^o, D_e^{eff} are constant within the negative electrode, separator, and positive electrode but can have different values in the three domains. Equation (2.6) has zero flux boundary conditions at the current collectors,

$$\left.\frac{\partial c_e}{\partial x}\right|_{x=0} = \left.\frac{\partial c_e}{\partial x}\right|_{x=L} = 0. \tag{2.7}$$

2.3.2 Conservation of Charge

Charge conservation in the solid phase of each electrode is described by Ohm's law

$$\sigma^{eff}\frac{\partial^2 \phi_s}{\partial x^2} - j = 0 \quad \text{for } x \in (0, L), \tag{2.8}$$

where $\phi_s(x,t)$ and σ^{eff} are the potential and effective conductivity of the solid matrix, respectively, with σ^{eff} evaluated from active material reference conductivity σ as $\sigma^{eff} = \sigma\varepsilon_s$. Conductivity is assumed constant in the negative electrode ($\sigma^{eff} = \sigma_-^{eff}$ for $x \in (0, \delta_-)$), the separator, and the positive electrode ($\sigma^{eff} = \sigma_+^{eff}$ for $x \in (\delta_- + \delta_{sep}, L)$). The boundary conditions at the current collectors are proportional to applied current,

$$-\sigma_-^{eff}\left.\frac{\partial \phi_s}{\partial x}\right|_{x=0} = \sigma_+^{eff}\left.\frac{\partial \phi_s}{\partial x}\right|_{x=L} = \frac{I}{A}, \tag{2.9}$$

where A is electrode plate area and *I(t)* is the applied current following the sign convention that a positive current discharges the battery. The boundary conditions at the separator require zero electronic current

$$\left.\frac{\partial \phi_s}{\partial x}\right|_{x=\delta_-} = \left.\frac{\partial \phi_s}{\partial x}\right|_{x=\delta_- + \delta_{sep}} = 0. \tag{2.10}$$

Electrolyte phase charge conservation yields

$$\kappa^{eff}\frac{\partial^2\phi_e}{\partial x^2}+\frac{\kappa_D^{eff}}{c_{e,0}}\frac{\partial^2 c_e}{\partial x^2}+j=0 \quad \text{for } x\in(0,L), \tag{2.11}$$

where $\phi_e(x,t)$ is the electrolyte phase potential and κ^{eff} the effective ionic conductivity, calculated from the Bruggeman relation $\kappa^{eff}=\kappa\varepsilon_e^p$.

The boundary conditions for Eq. (2.11) are zero flux at the two current collectors,

$$\left.\frac{\partial\phi_e}{\partial x}\right|_{x=0}=\left.\frac{\partial\phi_e}{\partial x}\right|_{x=L}=0. \tag{2.12}$$

At the electrode separator interfaces, we have flux continuity as

$$\left.\left(\kappa^{eff}\frac{\partial\phi_e}{\partial x}+\kappa_D^{eff}\frac{\partial c_e}{\partial x}\right)\right|_{int_-}=\left.\left(\kappa^{eff}\frac{\partial\phi_e}{\partial x}+\kappa_D^{eff}\frac{\partial}{\partial x}c_e\right)\right|_{int_+}, \tag{2.13}$$

where $int=\delta_-$ and $\delta_-+\delta_{sep}$ corresponding to the two separator interfaces.

2.3.3 Reaction Kinetics

The four governing PDEs (2.3), (2.6), (2.8), and (2.11) describing field variables, $c_{s,e}(x,t)$, $c_e(x,t)$, $\phi_s(x,t)$, and $\phi_e(x,t)$, are coupled by the Butler-Volmer electrochemical kinetic expression

$$j=i_0\left\{\exp\left[\frac{\alpha_a F}{RT}\eta\right]-\exp\left[-\frac{\alpha_c F}{RT}\eta\right]\right\} \quad \text{for } x\in(0,L), \tag{2.14}$$

where $i_0(x,t)$ is the exchange current density, $\eta(x,t)$ is the overpotential, and α_a and α_c are the anodic and cathodic transfer coefficients, respectively. The exchange current density is related to both solid surface and electrolyte concentrations according to

$$i_0=k(c_e)^{\alpha_a}(c_{s,\max}-c_{s,e})^{\alpha_a}(c_{s,e})^{\alpha_c} \quad \text{for } x\in(0,L), \tag{2.15}$$

where k is a kinetic rate constant and $c_{s,\max}$ is the maximum solid phase Li concentration. In Eq. (2.14), j is driven by overpotential, defined as the difference between solid and electrolyte phase potentials minus the thermodynamic equilib-

rium potential, U, of the solid phase,

$$\eta = \phi_s - \phi_e - U \quad \text{for } x \in (0, L). \tag{2.16}$$

Equilibrium potential, $U(c_{s,e})$, is evaluated as a function of the solid phase concentration at the particle surface and has different values in the two electrodes.

2.3.4 Cell Voltage

With boundary conditions applied galvanostatically as in Eq. (2.9), cell current, $I(t)$, is the model input. Voltage across the cell terminals is calculated from

$$V(t) = \phi_s(L, t) - \phi_s(0, t) - \tfrac{R_f}{A} I(t) \tag{2.17}$$

where R_f is an empirical contact resistance.

2.4 Impedance model formulation

2.4.1 Linearization

The Butler-Volmer Eq. (2.14) must be linearized at an equilibrium point in order to produce a linear model. As a first step in the linearization process, the equilibrium distributions for concentrations and potentials are calculated. At equilibrium, the currents $j = I = 0$ so $\eta = 0$ from the Butler-Volmer equation and constant distributions (independent of space and time) satisfy the governing equations. Specifically, $c_s(r, t) = \bar{c}_s =$ constant (independent of r and t) satisfies conservation of Li in the solid phase Eq. (2.3) and boundary conditions (2.4) and (2.5) because $\dot{\bar{c}}_s = 0$. Thus, the equilibrium Li concentration is uniform throughout the particle and surface concentration equals the average concentration so $c_{se}(x, t) = c_s(r, t) = \bar{c}_s$. Similarly, conservation of Li in the electrolyte phase Eq. (2.6) and boundary conditions (2.7) are satisfied with $c_e(x, t) = \bar{c}_e =$ constant (independent of x and t). It is safe to assume that $\bar{c}_e = 0$ because in equilibrium the Li ions are stored in either the positive or negative electrode with very few remaining in the electrolyte. Charge concentration in the solid phase at equilibrium is also constant with $\phi_s(x, t) = \bar{\phi}_s$.

A constant electrolyte potential $\phi_e(x,t) = \bar{\phi}_e$ satisfies charge concentration in the electrolyte phase in equilibrium.

From the definition of overpotential in Eq. (2.16), we have the equilibrium relationships

$$\bar{\phi}_s^- = \bar{U}^- + \bar{\phi}_e, \tag{2.18}$$

$$\bar{\phi}_s^+ = \bar{U}^+ + \bar{\phi}_e, \tag{2.19}$$

where $\bar{U} = U(\bar{c}_s)$. If we assign the negative terminal as ground then $\bar{\phi}_s^- = 0$, $\bar{\phi}_e = -\bar{U}^-$ and

$$\bar{V} = \bar{\phi}_s^+ = \bar{U}^+ - \bar{U}^- \tag{2.20}$$

equals the open circuit voltage.

In summary, the equilibrium variables for a Li-Ion cell are determined by the specified or given value of the average concentration $\bar{c}_s$. Knowing $\bar{c}_s$ is equivalent to knowing the State of Charge (SOC) of the cell. Given the SOC or $\bar{c}_s$, the equilibrium values of V, ϕ_s, and ϕ_e can all be calculated.

The second step in linearization is to use perturbation equations that set each variable equal to its equilibrium value plus a small deviation indicated by the variable with a tilde on top (*e.g.* $c_s(x,t) = \bar{c}_s + \tilde{c}_s(x,t)$ where $\tilde{c}_s(x,t)$ is small). For the variables with zero equilibrium values ($\eta(x,t)$, $c_e(x,t)$, $j(x,t)$, and ϕ_s^-) the tilde variables equal the original values (*e.g.* $\eta(x,t) = \tilde{\eta}(x,t)$) so we leave off the tildes for simplicity.

Substitution of the perturbation equations into the governing equations, expanding nonlinear terms using a Taylor series, canceling the equilibrium terms, and keeping only first order terms in the tilde variables results in a set of linear equations. For the Li-Ion model, all of the equations are linear with the exception of the Butler-Volmer Eq. (2.14) and the overpotential Eq. (2.16). For the linear equations, one can simply substitute all variables with tilde variables to obtain the "linearized" equations. The nonlinear Eq. (2.14) linearizes to

$$\eta = \frac{R_{ct}}{a_s} j, \tag{2.21}$$

with charge transfer resistance, $R_{ct} = \frac{RT}{\bar{i}_0 F(\alpha_a + \alpha_c)}$ and $\bar{i}_0$ is calculated at $c_e = 0$ and

$c_{s,e} = \bar{c}_s$. Eq. (2.16) linearizes to

$$\eta = \tilde{\phi}_s - \tilde{\phi}_e - \tilde{U} \tag{2.22}$$

where

$$\tilde{U} = \frac{\partial U}{\partial c}\tilde{c}_{s,e} \tag{2.23}$$

with

$$\frac{\partial U}{\partial c} = \left.\frac{\partial U}{\partial c_{s,e}}\right|_{c_{s,e}=\bar{c}_s} \tag{2.24}$$

assumed constant.

2.4.2 Impedance Solution

For the pseudo-2D model of a Li-Ion cell presented here, the embedded particles complicate the problem to the point where an analytical solution is not possible. In this section, we neglect electrolyte diffusion in order to obtain an analytical solution for the remaining variables, including the current density distribution $j(x,t)$. Using this distribution as input to an FEM model of electrolyte diffusion allows an approximate inclusion of this important effect. The approach presented in this section follows that of [19].

The linearized particle diffusion equation is

$$\frac{\partial \tilde{c}_s}{\partial t} = \frac{D_s}{r^2}\frac{\partial}{\partial r}\left(r^2\frac{\partial \tilde{c}_s}{\partial r}\right) \tag{2.25}$$

with the boundary conditions

$$\left.\frac{\partial \tilde{c}_s}{\partial r}\right|_{r=0} = 0 \tag{2.26}$$

and

$$D_s \left.\frac{\partial \tilde{c}_s}{\partial r}\right|_{r=R_s} = -\frac{j}{F}. \tag{2.27}$$

Taking Laplace Transform of Eq. (2.25) subject to the boundary conditions yields the transfer function [49]

$$\frac{\tilde{C}_{s,e}(x,s)}{J(x,s)} = \frac{1}{F}\left(\frac{R_s}{D_s}\right)\left[\frac{\tanh(\beta)}{\tanh(\beta)-\beta}\right] = \mathcal{G}_p(s), \tag{2.28}$$

where $\tilde{C}_{s,e}(x,s)$ and $J(x,s)$ are the Laplace Transforms of $\tilde{c}_{s,e}(x,t)$ and $j(x,t)$, respectively, and $\beta = R_s\sqrt{\frac{s}{D_s}}$.

The Laplace Transform of the linearized Butler-Volmer Eq. (2.21) is

$$\mathcal{N}(x,s) = \frac{R_{ct}}{a_s} J(x,s), \tag{2.29}$$

where $\mathcal{N}(x,s) = \mathcal{L}\{\eta(x,t)\}$.

If we neglect electrolyte diffusion, then the remaining variables of interest are ($c_{s,e}$, ϕ_e, and ϕ_s). Under this assumption, the positive and negative electrodes are decoupled from one another. The separator does not contribute to the analytical solution because there are no particles or electrodes. We therefore seek analytical solutions for $c_{s,e}$, ϕ_e, and ϕ_s in a single electrode and define the dimensionless spatial variable $z = \frac{x}{\delta}$, where δ is the electrode thickness and $z = 0$ and 1 at the current collector and separator interfaces, respectively.

The Laplace Transform of the solid phase charge conservation Eq. (2.8) is

$$\frac{\sigma^{eff}}{\delta^2}\frac{\partial^2 \tilde{\Phi}_s(z,s)}{\partial z^2} - J(z,s) = 0 \tag{2.30}$$

with $x \to z$. The boundary conditions are

$$-\frac{\sigma^{eff}}{\delta}\frac{\partial \tilde{\Phi}_s}{\partial z}\bigg|_{z=0} = \frac{\mathcal{I}}{A}, \tag{2.31}$$

where $\mathcal{I}(s) = \mathcal{L}\{I(t)\}$ and

$$\frac{\partial \tilde{\Phi}_s}{\partial z}\bigg|_{z=1} = 0 \tag{2.32}$$

Neglecting electrolyte diffusion, the Laplace Transform of the electrolyte charge conservation Eq. (2.11) becomes

$$\frac{\kappa^{eff}}{\delta^2}\frac{\partial^2 \tilde{\Phi}_e}{\partial z^2} + J = 0 \tag{2.33}$$

with the boundary condition at the current collector

$$\left.\frac{\partial\tilde{\Phi}_e}{\partial z}\right|_{z=0} = 0. \tag{2.34}$$

The boundary condition at the separator can be obtained by integration of the charge conservation equation over the domain, or, equivalently, enforcing charge conservation in the electrode as a whole. Integration of the solid phase charge conservation Eq. (2.30)

$$\int_0^1 J dz = \int_0^1 \frac{\sigma^{eff}}{\delta^2}\frac{\partial^2\tilde{\Phi}_s}{\partial z^2}dz = \frac{\sigma^{eff}}{\delta^2}\left.\frac{\partial\tilde{\Phi}_s}{\partial z}\right|_0^1 = -\frac{\mathcal{I}}{A\delta}, \tag{2.35}$$

using the boundary conditions. From liquid phase charge conservation, Eq. (2.33),

$$\int_0^1 J dz = -\int_0^1 \frac{\kappa^{eff}}{\delta^2}\frac{\partial^2\tilde{\Phi}_e}{\partial z^2}dz = -\frac{\kappa^{eff}}{\delta^2}\frac{\partial\tilde{\Phi}_e}{\partial z}(1,s), \tag{2.36}$$

using the zero flux boundary condition at $z = 0$. Equating Eqs. (2.35) and (2.36) provides the missing boundary condition on electrolyte phase potential at the separator,

$$\frac{\kappa^{eff}}{\delta}\frac{\partial\tilde{\Phi}_e}{\partial z}(1,s) = \frac{\mathcal{I}}{A}. \tag{2.37}$$

The last equation needed for the analytical solution is the Laplace Transform of Eq. (2.22)

$$\mathcal{N} = \tilde{\Phi}_s - \tilde{\Phi}_e - \frac{\partial U}{\partial c}\tilde{C}_{s,e} \tag{2.38}$$

which depends only on the difference between the solid and electrolyte phase potentials $\tilde{\Phi}_{s-e} = \Phi_s - \tilde{\Phi}_e$. Combining Eqs. (2.30) and (2.33), we obtain

$$\frac{\partial^2\tilde{\Phi}_{s-e}}{\partial z^2} = \delta^2\left(\tfrac{1}{\kappa^{eff}} + \tfrac{1}{\sigma^{eff}}\right)J \tag{2.39}$$

with boundary conditions

$$-\frac{\sigma^{eff}}{\delta}\frac{\partial\tilde{\Phi}_{s-e}}{\partial z}(0,s) = \frac{\kappa^{eff}}{\delta}\frac{\partial\tilde{\Phi}_{s-e}}{\partial z}(1,s) = \frac{\mathcal{I}}{A}, \tag{2.40}$$

obtained by combining the solid and electrolyte phase potential boundary conditions.

Eq. (2.38) can be simplified using the transfer function (2.28) and linearized Butler-Volmer (2.29) to produce

$$\tilde{\Phi}_{s-e} = \left[R_{ct} + \frac{\partial U}{\partial c} \mathcal{G}_p \right] \tilde{J}. \tag{2.41}$$

Combining Eqs. (2.39) and (2.41), we obtain a single ODE

$$\frac{\partial^2 \tilde{\Phi}_{s-e}}{\partial z^2} - \delta^2 \left(\tfrac{1}{\kappa^{eff}} + \tfrac{1}{\sigma^{eff}} \right) \left[R_{ct} + \frac{\partial U}{\partial c} \mathcal{G}_p(s) \right]^{-1} \tilde{\Phi}_{s-e} = 0, \tag{2.42}$$

with boundary conditions (2.40) in the single unknown $\tilde{\Phi}_{s-e}(x, s)$. The beauty of the transfer function approach taken here is that in the ODE (2.42) the Laplace variable s is a parameter so one need only solve the linear, constant parameter equation,

$$\frac{\partial^2 \tilde{\Phi}_{s-e}}{\partial z^2} - \nu^2 \tilde{\Phi}_{s-e} = 0, \tag{2.43}$$

where

$$\nu(s) = \delta \left(\tfrac{1}{\kappa^{eff}} + \tfrac{1}{\sigma^{eff}} \right)^{\frac{1}{2}} \left[R_{ct} + \frac{\partial U}{\partial c} \mathcal{G}_p(s) \right]^{-\frac{1}{2}} \tag{2.44}$$

is independent of $\tilde{\Phi}_{s-e}$ (linear) and z (constant parameter).

The solutions of Eq. (2.43) are exponentials of the form

$$\tilde{\Phi}_{s-e}(z, s) = C_1(s) \sinh\left[\nu(s)\ z\right] + C_2(s) \cosh\left[\nu(s)\ z\right]. \tag{2.45}$$

Substitution of Eq. (2.45) into the boundary conditions (2.40) yields the coefficients

$$\frac{C_1(s)}{\mathcal{I}(s)} = -\frac{\delta}{\nu(s) A \sigma^{eff}}, \tag{2.46}$$

$$\frac{C_2(s)}{\mathcal{I}(s)} = \frac{\delta \left(\kappa^{eff} \cosh(v(s)) + \sigma^{eff} \right)}{A \kappa^{eff} \sigma^{eff} \nu(s) \sinh(v(s))}. \tag{2.47}$$

Substitution of the coefficients (2.46) into Eq. (2.45) yields

$$\frac{\tilde{\Phi}_{s-e}(z,s)}{\mathcal{I}(s)} = \frac{\delta}{A\nu \sinh \nu} \left\{ \frac{1}{\sigma^{eff}} \cosh\left[\nu\,(z-1)\right] + \frac{1}{\kappa^{eff}} \cosh\left[\nu\; z\right] \right\}. \tag{2.48}$$

Using Eq. (2.41), we obtain the transfer function

$$\begin{aligned} \frac{J(z,s)}{\mathcal{I}(s)} =& \frac{J(z,s)}{\tilde{\Phi}_{s-e}(z,s)} \frac{\tilde{\Phi}_{s-e}(z,s)}{\mathcal{I}(s)} = \frac{\nu^2 \sigma^{eff} \kappa^{eff}}{\delta^2(\sigma^{eff}+\kappa^{eff})} \frac{\tilde{\Phi}_{s-e}(z,s)}{\mathcal{I}(s)} \\ =& \frac{\nu}{\delta A(\kappa^{eff}+\sigma^{eff}) \sinh \nu} \left\{ \kappa^{eff} \cosh\left[\nu\,(z-1)\right] + \sigma^{eff} \cosh\left[\nu\,(z)\right] \right\}. \end{aligned} \tag{2.49}$$

From Eq. (2.29), we have

$$\frac{\mathcal{N}(z,s)}{\mathcal{I}(s)} = R_{ct} \frac{J(z,s)}{\mathcal{I}(s)} \tag{2.50}$$

and using Eq. (2.28),

$$\frac{\tilde{C}_{s,e}(z,s)}{\mathcal{I}(s)} = \frac{\tilde{C}_{s,e}(s)}{J(s)} \frac{J(z,s)}{\mathcal{I}(s)}, \tag{2.51}$$

both of which use the transfer function (2.49).

2.4.3 FEM Electrolyte Diffusion

Now we reintroduce electrolyte diffusion using a FEM model that allows relaxation of the simplifying assumption used to obtain an analytical solution in the previous section. The current density solution in Eq. (2.49) is the input to a FEM electrolyte diffusion model. Electrolyte diffusion correction terms are calculated using the FEM model that add the effects of electrolyte diffusion to electrolyte potential and hence voltage.

Eq. (2.6) governing conservation of Li in the electrolyte was not used in the impedance model and the concentration coupling term in the electrolyte Eq. (2.11) was neglected. Using the FEM method described in Appendix, we discretize these two equations to

$$\mathbf{M}\dot{\mathbf{c}}_e = -\mathbf{K}\mathbf{c}_e + \mathbf{F}\mathbf{j} \tag{2.52}$$

and

$$\mathbf{K}_\phi \boldsymbol{\phi}_e + \mathbf{K}_c \mathbf{c}_e(t) = \mathbf{F}_\phi \mathbf{j}, \tag{2.53}$$

where $\mathbf{c}_e(t)$ and $\boldsymbol{\phi}_e(x,t)$ are the nodal electrolyte concentrations $\tilde{c}_e(x_i,t)$ and potentials $\tilde{\phi}_e(x_i,t)$ and

$$\mathbf{j}^T(t) = \left[j_-(x_1,t), \ldots j_-(x_{n_-},t), 0, \ldots 0,\ j_+(x_{n_{cell}-n_++1},t), \ldots j_+(x_{n_{cell}},t)\right] \quad (2.54)$$

is the current density calculated at the n_- nodal points in the negative electrode and n_+ nodal points in the positive electrode using the transfer function (2.49). The current density is zero for the nodal points in the separator.

The electrolyte concentration distribution is calculated by taking the Laplace transform of Eq. (2.52) and solving for $\mathbf{C}_e(s) = \mathcal{L}(\mathbf{c}_e(t))$ as

$$\frac{\mathbf{C}_e(s)}{\mathcal{I}(s)} = (\mathbf{K} + s\mathbf{M})^{-1}\mathbf{F}\mathbf{J}, \quad (2.55)$$

where $\mathbf{J}_i = J(z_i,s)/\mathcal{I}(s)$.

Solution of the discretized electrolyte potential Eq. (2.53) requires inversion of the matrix $\mathbf{K}_\phi$. This matrix is singular, however, due to the zero flux boundary conditions at $x = 0$ and L. To avoid this problem, we define voltages relative to $\phi_e(0,t)$ so that $\Delta\phi_e(x,t) = \phi_e(x,t) - \phi_e(0,t)$ is calculated. Relative potential is all that is required to calculate the voltage. It is not possible to enforce both $\Delta\phi_e(0,t) = 0$ and $\Delta\phi_e'(0,t) = 0$ for a second order ODE, however, so we approximate this by subtracting the (1,1) element of $\mathbf{K}_\phi$ from the first column of all rows of $\mathbf{K}_\phi$ as follows

$$\mathbf{K}_{\Delta\phi} = \mathbf{K}_\phi - (\mathbf{K}_\phi)_{1,1}\begin{bmatrix} 1 & 0 & \cdots & 0 \\ 1 & 0 & & \\ \vdots & & \ddots & \\ 1 & 0 & \cdots & 0 \end{bmatrix}, \quad (2.56)$$

to produce an approximation of

$$\frac{\Delta\boldsymbol{\Phi}_e(s)}{\mathcal{I}(s)} = (\mathbf{K}_{\Delta\phi})^{-1}\left(-\mathbf{K}\frac{\Delta\mathbf{C}_e(s)}{\mathcal{I}(s)} + \mathbf{F}\frac{\Delta\mathbf{J}}{\mathcal{I}(s)}\right). \quad (2.57)$$

where $\Delta\mathbf{C}_e = \mathbf{C}_e - (\mathbf{C}_e)_{1,1}$ and $\Delta\mathbf{J} = \mathbf{J} - (\mathbf{J})_{1,1}$.

2.4.4 Overall System Transfer Function

The voltage Eq. (2.17) can be expanded as

$$\tilde{V}(t) = \tilde{\phi}_e(L,t) - \tilde{\phi}_e(0,t) + \eta(L,t) - \eta(0,t) + \frac{\partial U^+}{\partial c}\tilde{c}_{s,e}(L,t) - \frac{\partial U^-}{\partial c}\tilde{c}_{s,e}(0,t) - \frac{R_f}{A}I(t). \quad (2.58)$$

After application of the Laplace Transform, the final, overall system impedance is

$$\frac{\tilde{V}(s)}{\mathcal{I}(s)} = \frac{\Delta\Phi_e(L,s)}{\mathcal{I}(s)} + \frac{\Delta\mathcal{N}(L,s)}{\mathcal{I}(s)} + \frac{\partial U^+}{\partial c}\frac{\tilde{C}_{s,e}(L,s)}{\mathcal{I}(s)} - \frac{\partial U^-}{\partial c}\frac{\tilde{C}_{s,e}(0,s)}{\mathcal{I}(s)} - \frac{R_f}{A}, \quad (2.59)$$

where $\Delta\Phi_e(L,s)$ is the n_{cell}^{th} element of $\Delta\mathbf{\Phi}_e(s)$ and $\Delta\mathcal{N}(x,s) = \mathcal{N}(x,s) - \mathcal{N}(0,s)$.

2.5 Single Particle Model

The single particle model is developed under two major assumptions

- Each electrode is represented by a single active spherical particle.
- The dynamics due to electrolyte diffusion is negligible.

From the linearized Butler-Volmer equation we get the transfer function relating the overpotential to the current

$$\frac{\mathcal{N}(s)}{I(s)} = \frac{R_{ct}}{a_s}\frac{J(s)}{I(s)} = \frac{R_{ct}}{a_s A\delta} \quad (2.60)$$

The solid phase diffusion impedance in the spherical active material particles is given by

$$\frac{\tilde{C}_{s,e}(s)}{I(s)} = \frac{C_{s,e}(s)}{J(s)}\frac{J(s)}{I(s)} = \frac{1}{a_s F A\delta}\left(\frac{R_s}{D_s}\right)\left[\frac{\tanh(\beta)}{\tanh(\beta) - \beta}\right], \quad (2.61)$$

Substituting Eqs. (2.60) and (2.61) into (2.59), we obtain the cell impedance

$$\begin{aligned}\frac{\tilde{V}(s)}{I(s)} = &-\frac{R_{ct_+}}{a_{s_+}}\frac{1}{A\delta_+} - \frac{R_{ct_-}}{a_{s_-}}\frac{1}{A\delta_-} \\ &+ \frac{\partial u}{\partial c_{s+}}\frac{1}{A\delta_+}\frac{R_s}{a_s F D_{s+}}\left[\frac{\tanh(\beta)}{\tanh(\beta)-\beta}\right] \\ &- \frac{\partial u}{\partial c_{s-}}\frac{1}{A\delta_-}\frac{R_s}{a_s F D_{s-}}\left[\frac{\tanh(\beta)}{\tanh(\beta)-\beta}\right] - \frac{R_f}{A}\end{aligned} \tag{2.62}$$

2.6 Capacity Modeling

The nominal capacity of a cell C is defined to be the maximum number of ampere-hours that can be drawn from the fully charged cell at room temperature and a slow (e.g. $C/30$) rate. The remaining capacity $C_r(t)$ is defined as the number of ampere-hours that can be drawn from the cell starting from the current time t, at room temperature, and at a $C/30$ rate.

The volume averaged Li concentration

$$c_{s_{\text{avg}}} = \frac{1}{V_s}\int c_s dV_s, \tag{2.63}$$

where $V_s = \pi R_s^3/3$ and $dV_s = 4 * \pi r^2 dr$. This volume integration yields:

$$\dot{c}_{s_{\text{avg}}} = \frac{3D_s}{R_s}\left[R_s^2 c_s'(R_s,t)\right] = -\frac{1}{\epsilon_s F} j_{\text{avg}} \tag{2.64}$$

using the boundary conditions in Equations (2.4) and (2.5). The average current density is obtained by averaging the conservation of charge equation (2.8):

$$j_{\text{avg}} = \int_0^{\delta} \sigma^{\text{eff}} \phi_s' = \frac{1}{\delta A} I \tag{2.65}$$

for both the positive and negative electrodes. Subsititing Eq. (2.65) into Eq. (2.64), the concentration dynamics become

$$\dot{c_{s_{\text{avg}}}} = \frac{1}{\delta A \epsilon_s F} I. \tag{2.66}$$

The State of Charge is defined as:

$$\text{SOC} = \frac{C_r(t)}{C} = -\frac{1}{C}\int_0^t I(\tau)d\tau, \tag{2.67}$$

assuming the initial SOC at $t-0$ is zero and $I(t)$ is the applied current with $I > 0$ during discharge. SOC can be defined as

$$\text{SOC} = \frac{\frac{c_{s\text{avg}}}{c_{s\text{max}}} - \theta_{0\%}}{\theta_{100\%} - \theta_{0\%}} \tag{2.68}$$

for the negative electrode, positive electrode, or average of the two to get SOC for the whole cell, where $\theta_{0\%}$ and $\theta_{100\%}$ are experimentally determined reference stoichiometries. Using Eqns. (2.67),(2.68), and (2.66), the capacity is defined as

$$C = \delta A \epsilon F c_{s_{\text{max}}} \left[\theta_{100\%} - \theta_{0\%}\right]. \tag{2.69}$$

Chapter 3

Model Discretization

3.1 Introduction

The transcendental transfer functions derived in Chapter 2 include non-polynomial functions such as hyperbolics and square roots. This chapter presents discretization techniques to reduce the infinite order models to a low order state space form. The impedance model with the distributed electrode particles and electrolyte diffusion is discretized using a pole/residue expansion and the single particle impedance model is discretized using a Padé approximation given by.

3.2 Pole/Residue Realization

To produce a standard transfer function in the form of a ratio of two polynomials in s, we use the real pole and residue series approximation.

$$\hat{G}(\theta, s) = \sum_{k=1}^{N} \frac{R_k}{s - p_k}, \tag{3.1}$$

where the model order N is given and the residues R_k and poles p_k are unknown. The parameter vector $\theta = [R_1, \ldots, R_N, p_1, \ldots, p_N]$. For stability, the poles are all negative. The residues, however, can take on either sign.

To obtain a low order but accurate approximation system identification techniques are used to find θ. For a given N, the θ that best matches the frequency

response of the transcendental transfer function is determined in a least squares sense by minimizing the sum of the squares of the errors. The cost function to be minimized is the sum of the squares of the errors between the complex frequency response data $G(i\omega_j)$ and the estimate $\hat{G}(\theta, i\omega_j)$,

$$e(\theta, \omega_j) = G(i\omega_j) - \hat{G}(\theta, i\omega_j), \tag{3.2}$$

where the frequency response data is provided at $j = 1, \ldots, N_{eval}$ frequencies with $N_{eval} > N/2$. The cost function

$$CF = \sum_{j=1}^{N_{eval}} \left([\Re \{e(\theta, \omega_j)\}]^2 + [\Im \{e(\theta, \omega_j)\}]^2 \right), \tag{3.3}$$

where $\Re$ and $\Im$ indicate the real and imaginary parts, respectively. The objective is to find θ that minimizes CF. The residuals are the error terms that are squared in Eq. (3.4),

$$\begin{aligned} r_j(\theta) = \Re \{e(\theta, \omega_j)\} = \Re \{G(i\omega_j)\} + \\ \sum_{k=1}^{N} \frac{R_k p_k}{p_k^2 + \omega_j^2} \text{ for } j = 1, \ldots, N_{eval} \\ r_j(\theta) = \Im \{e(\theta, \omega_j)\} = \Im \{G(i\omega_j)\} + \\ \sum_{k=1}^{N} \frac{R_k \omega_j}{p_k^2 + \omega_j^2} \text{ for } j = N_{eval} + 1, \ldots, 2N_{eval} \end{aligned} \tag{3.4}$$

where the first N_{eval} $r_j(\theta)$ are associated with the real parts of the error and the last N_{eval}, the imaginary parts. Eq. (3.4) shows that the residuals are linear in R_k but nonlinear in p_k.

The Jacobian, $\mathbf{J} \in \Re^{2N_{eval} \times 2N}$, is the gradient of the residuals of the cost function with respect to the model parameters θ. Considering R_k as the only unknown parameter, the Jacobian

$$\mathbf{J}_R(j,k) = \frac{\partial r_j}{\partial R_k} = \begin{cases} \frac{p_k}{p_k^2 + \omega_j^2} & \text{for } j = 1, \ldots, N_{eval} \\ \\ \frac{\omega_j}{p_k^2 + \omega_j^2} & \text{for } j = N_{eval} + 1, \ldots, 2N_{eval} \end{cases} \tag{3.5}$$

for $k = 1, \ldots N$ is in $\Re^{2N_{eval} \times N}$ and independent of R_k but dependent on p_k. For p_k, the Jacobian

$$\mathbf{J}_p(j,k) = \frac{\partial r_j}{\partial p_k} = \begin{cases} \frac{R_k\left(\omega_j^2 - p_k^2\right)}{\left(p_k^2+\omega_j^2\right)^2} \\ \text{for } j = 1, \ldots, N_{eval}, \\ -\frac{2R_k p_k \omega_j}{\left(p_k^2+\omega_j^2\right)^2} \\ \text{for } j = N_{eval}+1, \ldots, 2N_{eval}, \end{cases} \tag{3.6}$$

for $k = 1, \ldots N$ is also in $\Re^{2N_{eval} \times N}$.

Solving for R_k if p_k is known constitutes a linear least squares problem because the Jacobian J_R is independent of R_j. We can rewrite the residuals as

$$\mathbf{r} = \begin{bmatrix} r_1 \\ \vdots \\ r_{2N_{eval}} \end{bmatrix} = \mathbf{g} - \mathbf{J}_R\mathbf{R}, \tag{3.7}$$

where $\mathbf{R} = [R_1, \ldots, R_N]'$, $\mathbf{g}(j) = \Re\{G(i\omega_j)\}$ for $j = 1, \ldots, N_{eval}$ and $\mathbf{g}_j = \Im\{G(i\omega_j)\}$ for $j = N_{eval}+1, \ldots, 2N_{eval}$. The cost function then becomes

$$CF = \left|\mathbf{g} - \mathbf{J}_R\mathbf{R}\right|^2. \tag{3.8}$$

The cost function in Eq. (3.8) is convex so the global minimum is at

$$\frac{\partial CF}{\partial \mathbf{R}} = 2{\mathbf{J}_R}^T\left(\mathbf{g} - \mathbf{J}_R\mathbf{R}\right) = 0, \tag{3.9}$$

producing the normal equations

$$\mathbf{J}_R{\mathbf{J}_R}^T\mathbf{R}^* = {\mathbf{J}_R}^T\mathbf{g}, \tag{3.10}$$

where $\mathbf{R}^*$ is the global minimizer of CF. If $\mathbf{J}_R{\mathbf{J}_R}^T$ is invertible then we can solve Eq. (3.10) directly for $\mathbf{R}^*$.

For the nonlinear least squares problem associated with finding the poles $\mathbf{p}$ there are many algorithms that can be used. In our approach we have used the matlab function which uses an algorithm that is explicitly designed for nonlinear

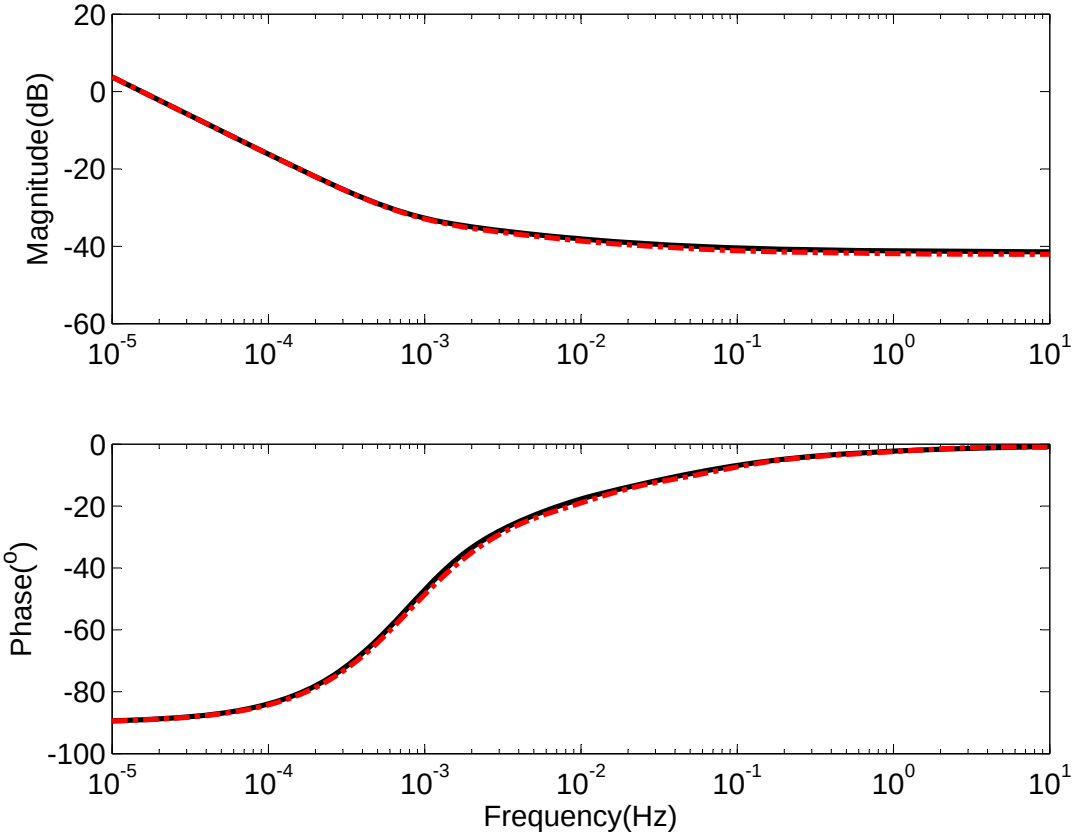

Figure 3.1. Frequency Response: Transcendental transfer function (black) vs Reduced order model (red).

least squares problems with an analytical Jacobian. The nonlinear optimization problem associated with finding the poles is not convex and there can be a large number of closely spaced minima. The poles are interchangeable so if two poles switch the error will be unchanged. The minimum that the function returns is very sensitive to the initial guess that is required by the algorithm.

Using the least squares optimization, a best fit eighth order (Reduced order(RO)) model was obtained and the algorithm was validated by comparing the frequency responses with the transcendental frequency response for a 3.1Ah Li-ion cell with parameters in Tab.3.3. The RO model was obtained to match the actual transfer function for a desired bandwidth upto 10 Hz as shown in Fig.3.1.

In many cases it is of interest to plot the time response of a distribution as snapshots of the variable plotted versus x at several different times t_i. This requires

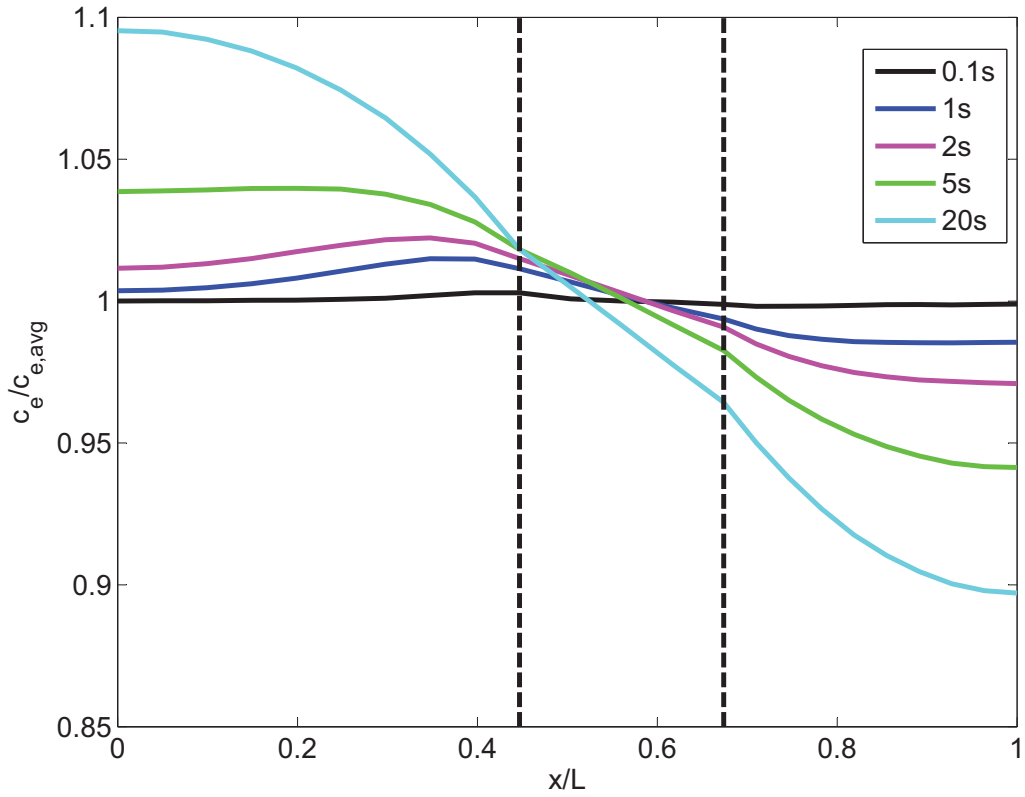

Figure 3.2. Electrolyte Concentration Distribution, $c_e(x,t)$, Time Response: 5C discharge from 60% SOC at various times

the development of transfer functions at multiple values of x that can be simulated in time. This was done for 25 points evenly distributed along the x axis for the $c_e(x,t)$, $c_{s,e}(x,t)$, and $j(x,t)$ transfer functions and the time responses are plotted in Figs. 3.2, 3.3, and 3.4, respectively, for a 5C (30A) discharge from 60% SOC initial condition. For 25 10th order approximations, the simulation model order for each plot is 250 states. Model order reduction could easily reduce the number of states because the dynamic characteristics of the transfer functions are very similar.

Fig.3.2 shows that electrolyte concentration, $c_e(x,t)$, does approach a steady state distribution due to offsetting source/sink terms in the $j(x,t)$ distribution in the negative/positive electrode regions. Surface concentrations $c_{s,e}(x,t)$ shown in Fig. 3.3, fall/rise in a distributed manner consistent with the time history of

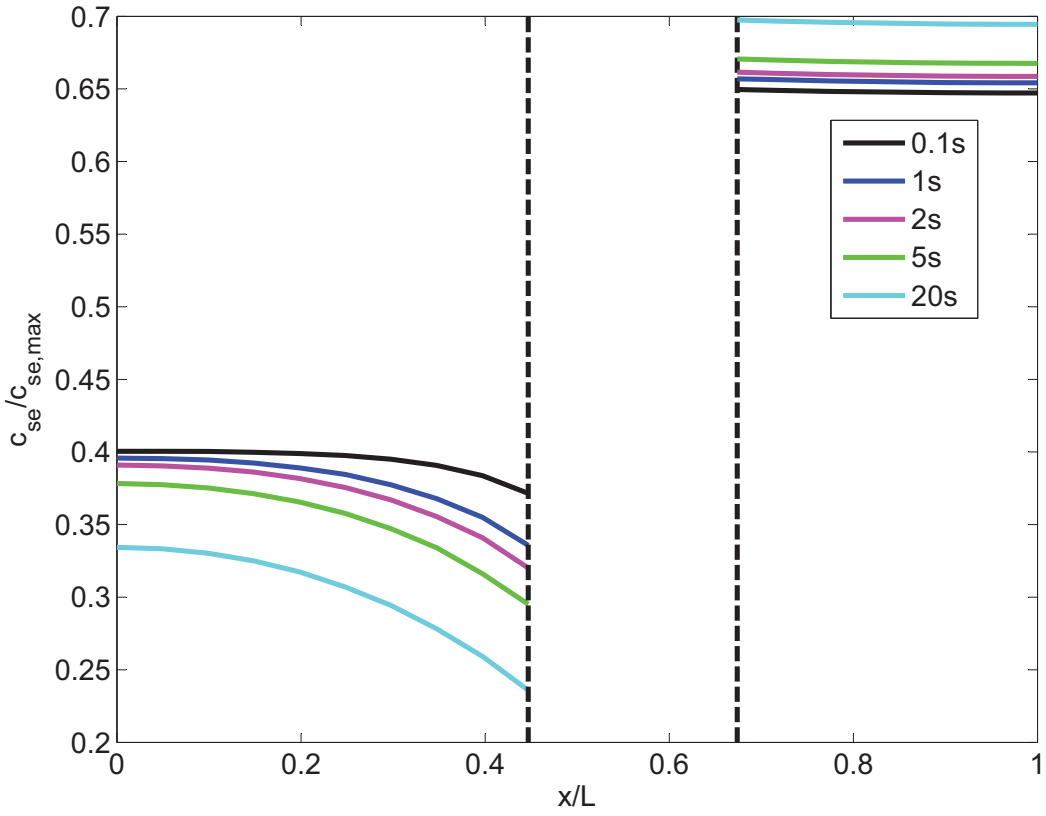

Figure 3.3. Solid Phase Surface Concentration Distribution, $c_{s,e}(x,t)$, Time Response: 5C discharge from 60% SOC at various times

current density, $j(x,t)$. While discharge continues, $c_{s,e}(x,t)$ continues to rise/fall and never reaches steady state due to an electrode bulk concentration integrator. As shown in Fig.3.4, initial spikes in reaction current, $j(x,t)$, near the separator decay as Li is de-inserted/inserted from the negative/positive electrode surface. Equilibrium potentials rise/fall most rapidly near the separator penalizing further reaction and over time $j(x,t)$ becomes more uniform.

3.3 Padé Approximation

The infinite dimensional single particle model is discretized by a Padé Approximation [50], [51]. The Padé Approximation works well for infinitely differentiable transfer functions that can be expanded in a power series at the origin. The N^{th}

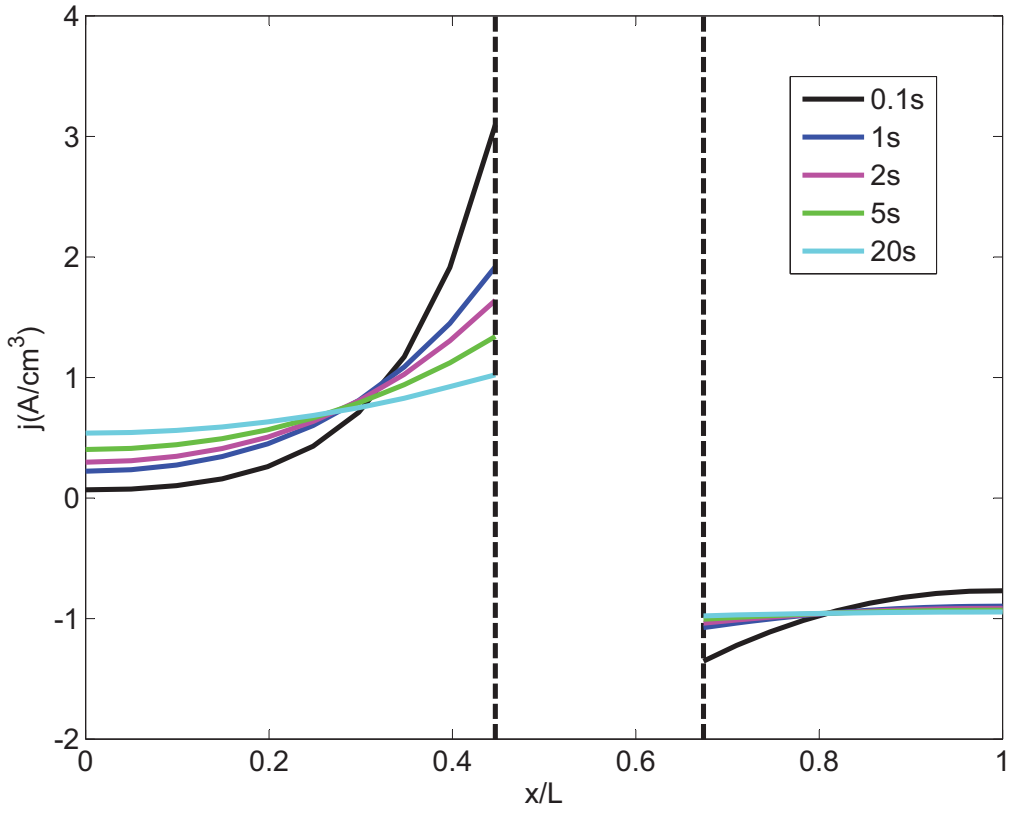

Figure 3.4. Current Density Distribution, $j(x,t)$, Time Response: 5C discharge from 60% SOC at various times.

order Padé approximation of a transfer function $G(s)$ is a ratio of two polynomials in s where the denominator is of order N. For a proper transfer function, the numerator is of order N or less. The Padé Approximation Method can produce transfer functions with numerators of order 1 to N but the highest accuracy is often obtained when the numerator order is N. One may also choose the numerator order to match asymptote. The computational speed of the model and any model-based estimators and controllers depend strongly on the number of integrators in the model or the order of the denominator. The order of the numerator, however, does not influence computational speed as significantly.

We assume that the transfer function can be expanded in a power series at the

origin as follows

$$G(s) = \sum_{k=0}^{2(N+1)} c_k \, s^k, \tag{3.11}$$

where the coefficients c_k are calculated by repeated differentiation of $G(s)$ and evaluation at $s = 0$,

$$c_k = \left. \frac{d^k \, G(s)}{ds^k} \right|_{s=0}. \tag{3.12}$$

If $G(s)$ has a pole at the origin then we apply the power series expansion to $G^*(s) = s \, G(s)$.

The N^{th} order Padé approximation transfer function

$$P(s) = \frac{\sum_{m=0}^{N} b_m \, s^m}{1 + \sum_{n=1}^{N} a_n \, s^n} = \frac{num(s)}{den(s)}, \tag{3.13}$$

where we assume that the denominator and numerator both have order N. To determine $P(s)$ we must calculate the $N+1$ b_m and N a_m coefficients. The zeroth order term in the denominator is assumed to have a unity coefficient to normalize the solutions. The $2N+1$ linear equations that can be solved for the coefficients are determined from the polynomial equation

$$den(s) \sum_{k=0}^{2(N+1)} c_k s^k - num(s) = 0, \tag{3.14}$$

where the coefficients c_k are known from the power series expansion. Eq. (3.14) produces a polynomial of order $2N(N+1)$ in s. The left hand side equals zero for all s so the coefficients must be zero. The first $N+1$ coefficients of s depend on both the unknown a_n and b_n coefficients. The remaining coefficients depend only on a_n. Thus, we set the coefficients of s^{N+2} to s^{2N+1} equal to zero to solve for $a_1, \ldots, a_N$. Then, we substitute these solutions $a_1, \ldots, a_N$ into the coefficients of s^0 to s^N and set them equal to zero to solve for $b_0, \ldots, b_N$. The order N chosen is the minimum value for which the best frequency response match is obtained between the transcendental and the reduced order transfer function in the desired low frequency range extending upto 10Hz. This value of N can be chosen by a simple trial and error approach.

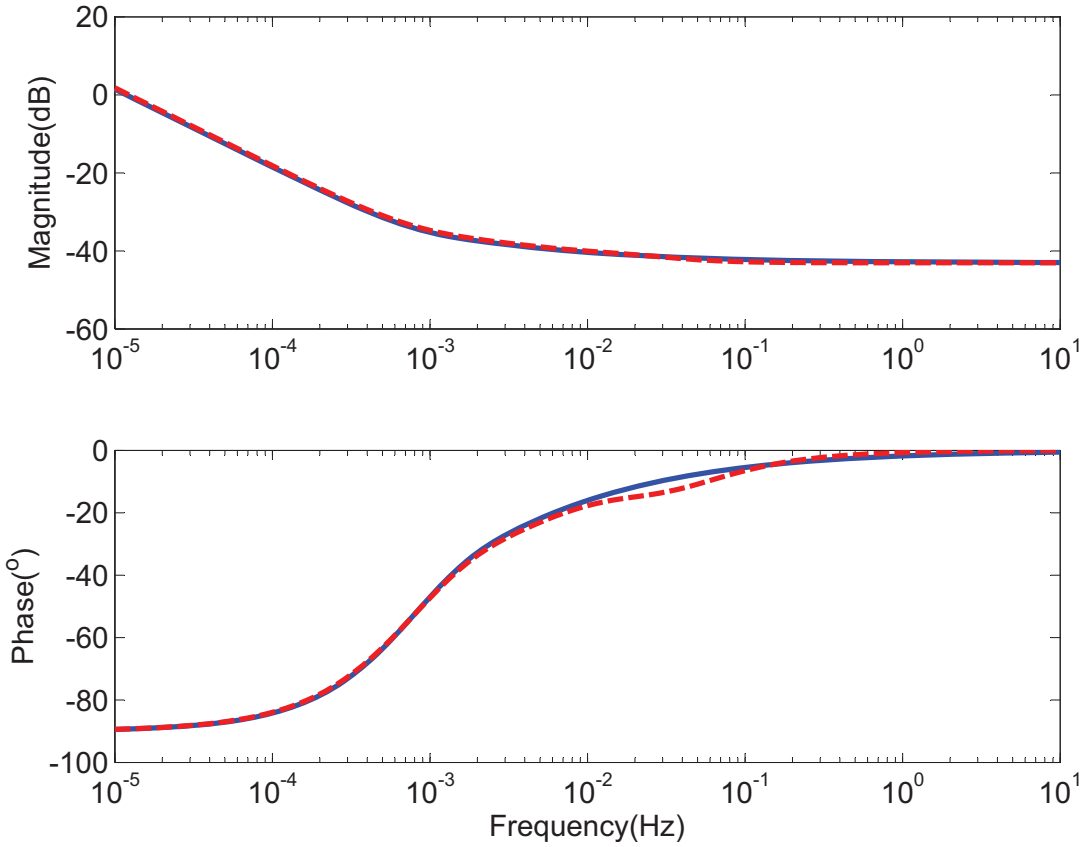

Figure 3.5. Frequency response: full order SP model (Blue) vs padé approximated SP model (red).

A third order Padé approximation is generated for each particle transfer function resulting in the SP model impedance transfer function

$$Z(s) = R_T + \frac{b_2 s^2 + b_1 s + b_0}{s^3 + a_2 s^2 + a_1 s} + \frac{d_2 s^2 + d_1 s + d_0}{s^3 + c_2 s^2 + c_1 s} \tag{3.15}$$

where the numerator and denominator coefficients are shown in Tab. 3.1 with

$$C^+ = \frac{\partial U^+}{\partial c_{s,e}^+},\ C^- = \frac{\partial U^-}{\partial c_{s,e}^-} \tag{3.16}$$

Table 3.1. Coefficient values

Numerator	Value	Denominator	Value
b_0	$\frac{10395C^+\left[D_s^+\right]^2}{AFa_s^+\delta_+\left[R_s^+\right]^5}$	a_0	0
b_1	$\frac{1260C^+D_s^+}{AFa_s^+\delta_+\left[R_s^+\right]^3}$	a_1	$\frac{3465\left[D_s^+\right]^2}{\left[R_s^+\right]^4}$
b_2	$\frac{21C^+}{AFa_s^+\delta_+R_s^+}$	a_2	$\frac{189D_s^+}{\left[R_s^+\right]^2}$
d_0	$\frac{10395C^-\left[D_s^-\right]^2}{AFa_s^-\delta_-\left[R_s^-\right]^5}$	c_0	0
d_1	$\frac{1260C^-D_s^-}{AFa_s^-\delta_-\left[R_s^+\right]^3}$	c_1	$\frac{3465\left[D_s^-\right]^2}{\left[R_s^-\right]^4}$
d_2	$\frac{21C^-}{AFa_s^-\delta_-R_s^-}$	c_2	$\frac{189D_s^-}{\left[R_s^-\right]^2}$

Equation (3.15) can be rewritten as

$$\begin{aligned} Z(s) = R_T + \frac{21\mathcal{C}^+s^2 + 1260\frac{\mathcal{C}^+}{\tau_D^+}s + 10395\frac{\mathcal{C}^+}{\tau_D^{+2}}}{s^3 + \frac{189}{\tau_D^+}s^2 + \frac{3465}{\tau_D^{+2}}s} \\ + \frac{21\mathcal{C}^-s^2 + 1260\frac{\mathcal{C}^-}{\tau_D^-}s + 10395\frac{\mathcal{C}^-}{\tau_D^{-2}}}{s^3 + \frac{189}{\tau_D^-}s^2 + \frac{3465}{\tau_D^{-2}}s}. \end{aligned} \tag{3.17}$$

The simplified transfer function (3.17) depends only on five independent parameters

$$\begin{aligned} R_T &= -\frac{R_{ct_+}}{a_{s_+}}\frac{1}{A\delta_+} - \frac{R_{ct_-}}{a_{s_-}}\frac{1}{A\delta_-} - \frac{R_f}{A} \\ \mathcal{C}^+ &= \frac{C^+}{AFa_s^+L^+R_s^+} = \frac{C_+}{3AF\delta_+\varepsilon_{s+}} \\ \tau_D^+ &= \frac{\left[R_s^+\right]^2}{D_s^+} \\ \mathcal{C}^- &= \frac{C^-}{AFa_s^-L^-R_s^-} = \frac{C_-}{3AF\delta_-\varepsilon_{s-}} \\ \tau_D^- &= \frac{\left[R_s^-\right]^2}{D_s^-}. \end{aligned}$$

where Q is the capacity of the battery and c_s is the solid phase concentration at the particular state of charge. The total resistance of the battery R_T results from the contact resistance and the charge transfer resistance in both electrodes. The capacity factors $\mathcal{C}$ are inversely proportional to the electrode volume fraction and directly proportional to the slope $\frac{\partial U}{\partial c_{s,e}}$. The diffusion times τ_D is directly proportional to the square of the particle radius and inversely proportional to the solid phase diffusion coefficient.

The impedance frequency response of the Padé approximated SP model is shown in Fig. (3.5). The Padé approximated model matched well for the desired 10 Hz bandwidth. The simplifying assumptions in the SP model are warranted if only impedance is desired. The SP model, however, cannot provide the distribution results shown in Figs. (3.2)-(3.4)

3.4 First Principles Equivalent Circuit Model

An advantage of the Padé approximated SP model is that the coefficients of the impedance transfer function are explicit functions of the physical parameters. This low order transfer function can be converted into an equivalent circuit with resistors and capacitors where the resistances and capacitances can be physically related to the model parameters. Fig. (3.6) shows an example equivalent circuit (the circuit realization is not unique) that combines four parallel RC circuits in series with a capacitor and a resistor.

The impedance of the equivalent circuit is

$$Z(s) = R_1 + \frac{1}{C_1 s} + \frac{\frac{1}{C_2}}{s + \frac{1}{R_2 C_2}} + \frac{\frac{1}{C_3}}{s + \frac{1}{R_3 C_3}} + \frac{\frac{1}{C_4}}{s + \frac{1}{R_4 C_4}} + \frac{\frac{1}{C_5}}{s + \frac{1}{R_5 C_5}}. \tag{3.18}$$

Equating Eq.(3.18) with the Padé approximated SP model transfer function Eq.(3.17) yields the explicit relationships between resistances and capacitances and physical parameters in Tab. (3.2).

Table 3.2. Circuit parameters in terms of cell parameters

Capacitor	Capacitance	Resistor	Resistance
C_1	$\frac{1}{3(\mathcal{C}^+ + \mathcal{C}^-)}$	R_1	R_T
C_2	$\frac{0.4583}{\mathcal{C}^+}$	R_2	$0.1071\mathcal{C}^+\tau_D^+$
C_3	$\frac{0.0632}{\mathcal{C}^+}$	R_3	$0.0945\mathcal{C}^+\tau_D^+$
C_4	$\frac{0.4583}{\mathcal{C}^-}$	R_4	$0.1071\mathcal{C}^-\tau_D^-$
C_5	$\frac{0.0632}{\mathcal{C}^-}$	R_5	$0.0945\mathcal{C}^-\tau_D^-$

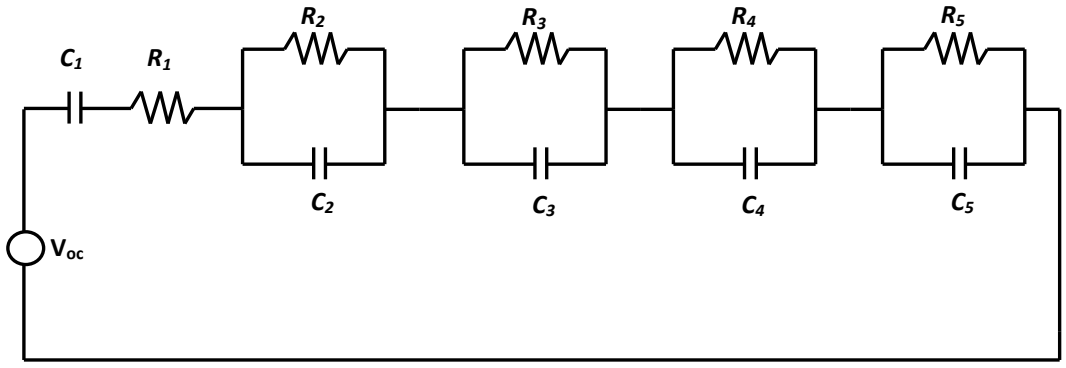

Figure 3.6. Equivalent circuit of a padé approximated single particle model.

3.5 Experimental Validation

The RO model and the Padé approximated SP model developed in the previous sections are experimentally validated in the frequency and time domains. Experimental electrochemical impedance spectroscopy (EIS) and pulse train time response data are collected from a commercial 3.1 Ah NCM battery. The model parameters shown in Tab. 3.3. A slow discharge/charge cycle is used to generate the OCP curve which is numerically differentiated to generate the $\frac{\partial U}{c_{s,e}}$ parameter. The contact resistance and the electrode plate area were tuned to match the 3.1 Ah capacity and experimental EIS data. Fig. 3.7 shows EIS measured for fresh cells after 1 hour rest following discharge from fully charged state at 1C-rate to 60% SoC. The impedance spectra are obtained with an AC amplitude of 5mV over a frequency range of 0.005 Hz to 50,000 Hz on a Solartron SI 1287 electrochemical

Table 3.3. Parameters for Li-Ion Cell Model.

PARAMETER	NEGATIVE	SEPARATOR	POSITIVE
Design Specifications			
Thickness, δ $[cm]$	50×10^{-4}	25.4×10^{-4}	43.5×10^{-4}
Particle radius, R_s $[cm]$	1×10^{-4}		1×10^{-4}
Polymer phase volume fraction, ε_p	0.048	0.5	0.110
Conductive filler volume fraction, ε_f	0.040		0.06
Porosity, ε_e	0.25	0.4	0.25
Electrode plate area, A $[cm^2]$	4504		
Li Ion Concentrations			
Maximum solid phase concentration $c_{s,max}$ $[mol\ cm^{-3}]$	16.1×10^{-3}		24.2×10^{-3}
Stoichiometry at 0% SOC, $x_{0\%}$	0.13		0.95
Stoichiometry at 100% SOC, $x_{100\%}$	0.68		0.34
Average electrolyte concentration, $c_{e,avg}$ $[mol\ cm^{-3}]$	1.2×10^{-3}		
Kinetic & Transport Properties			
Exchange current density, i_o $[A\ cm^{-2}]$	3.6×10^{-3}		2.6×10^{-3}
Charge-transfer coefficients, α_a, α_c	0.5, 0.5		0.5, 0.5
Solid phase Li diffusion coefficient, D_s $[cm^2\ s^{-1}]$	2.0×10^{-12}		9.9×10^{-12}
Solid phase conductivity, σ $[S\ cm^{-1}]$	1.0		0.1
Bruggeman porosity exponent, p	1.5	1.5	1.5
Electrolyte phase Li+ diffusion coefficient, D_e $[cm^2\ s^{-1}]$	2.6×10^{-6}		
Electrolyte phase ionic conductivity, κ $[S\ cm^{-1}]$	$\kappa = 0.0063$		
Electrolyte activity coefficient, $f_\pm$	1.0		
Li+ transference number, t_+^o	0.363		

interface coupled with Solartron SI 1255B frequency response analyzer. The model frequency responses extends to lower frequencies not measured experimentally due to equipment and testing time constraints. The experimental data includes frequencies higher than the 10 Hz bandwidth of the models. For the frequency range from 0.01 Hz to 10 Hz the agreement is quite good.

Pulse discharge and charge tests at 60% SoC and 2C, 5C and 10C rates are conducted on an Arbin BT-2000 battery cycler for 2s, 10s and 30s pulse durations. Fig. 3.8 shows that the model matches the experiment very well for the low currents of 2C and 5C but has significant error at the higher 10C current due to the linearization of the Butler Volmer equation.

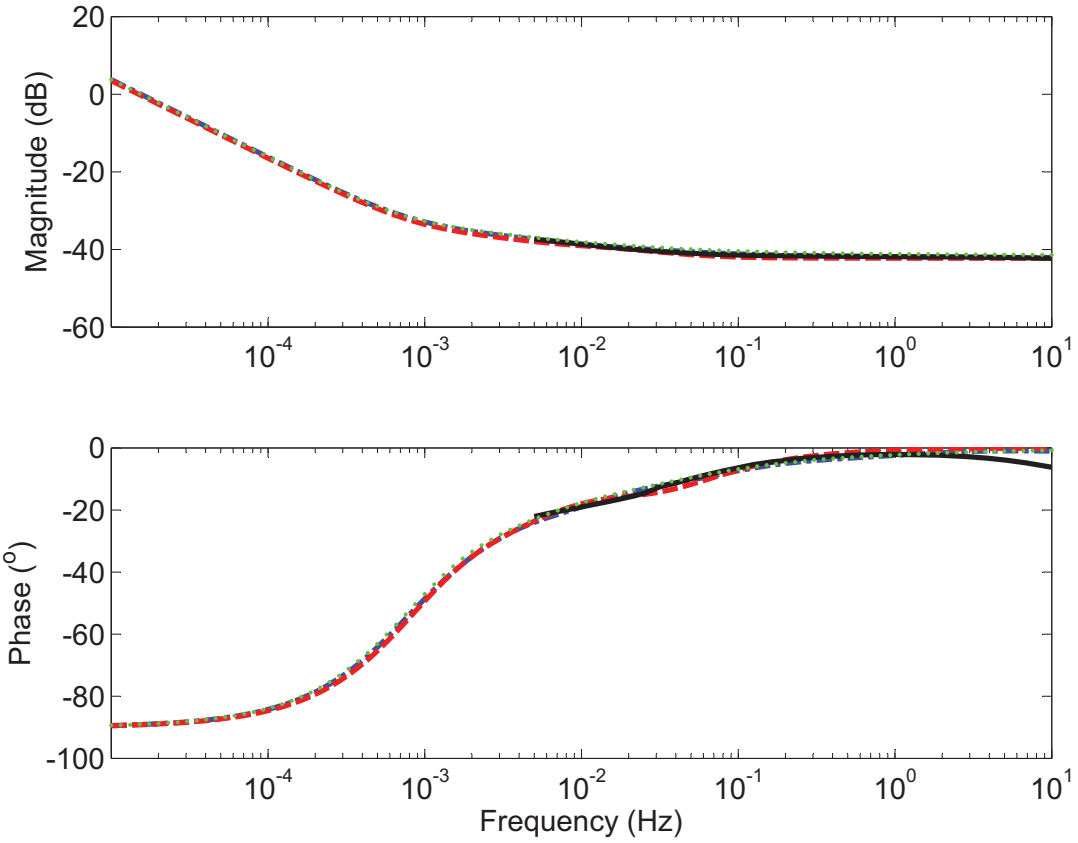

Figure 3.7. Impedance frequency response: transcendental transfer function (green-dotted), reduced order model (blue dash-dotted), padé approximated single particle model (red dashed), and experimental EIS (green-dotted).

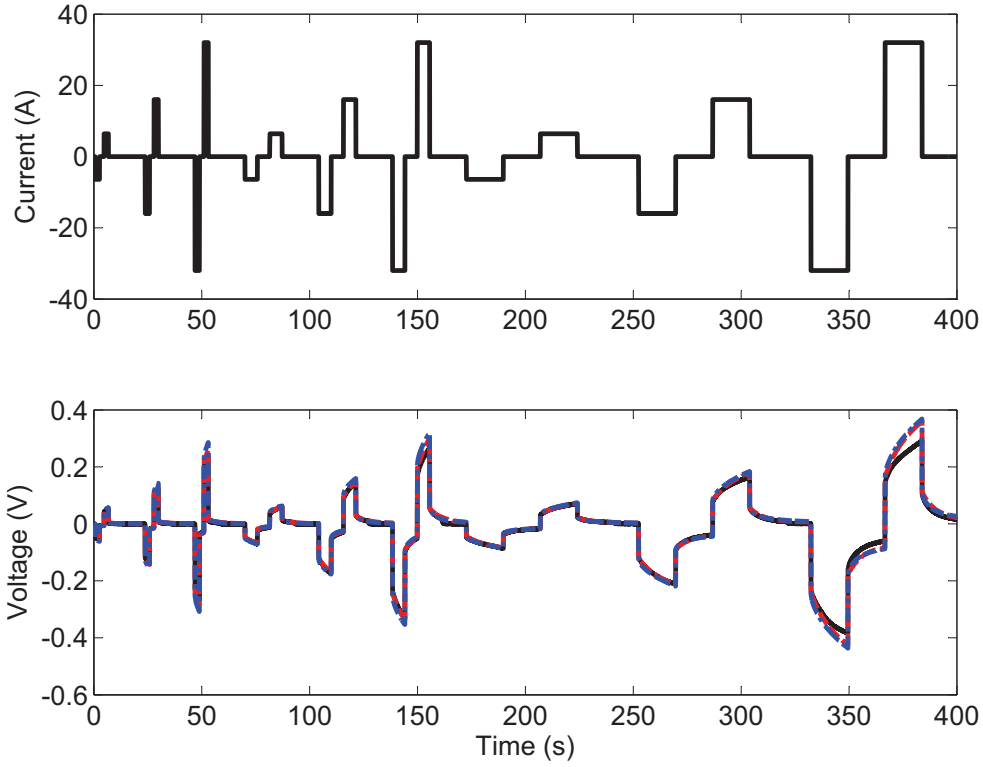

Figure 3.8. Experimental (black-solid),single particle model (red-dashed) and reduced order model(blue-dashed) pulse charge/discharge time response.

Chapter 4

State of Health Estimation

4.1 Introduction

This chapter describes techniques to estimate the State of Health (SOH) of a lithium ion battery from current voltage measurements using the single particle model. The aging parameters incorporated within the model is estimated via a least squares method for both $LiNi_{1/3}Co_{1/3}Mn_{1/3}O_2$ (NCM) and $LiFePO_4$ (LFP) chemistries and their variation is correlated to the degradation mechanisms responsible for the capacity fade and impedance rise in these cells. An online recursive parameter estimator is also designed using a gradient update method.

From Chapter 3 the Padé approximated single particle model is given by

$$\begin{aligned} Z(s) = R_T + \frac{21\mathcal{C}^+ s^2 + 1260\frac{\mathcal{C}^+}{\tau_D^+}s + 10395\frac{\mathcal{C}^+}{\tau_D^{+2}}}{s^3 + \frac{189}{\tau_D^+}s^2 + \frac{3465}{\tau_D^{+2}}s} \\ + \frac{21\mathcal{C}^- s^2 + 1260\frac{\mathcal{C}^-}{\tau_D^-}s + 10395\frac{\mathcal{C}^-}{\tau_D^{-2}}}{s^3 + \frac{189}{\tau_D^-}s^2 + \frac{3465}{\tau_D^{-2}}s}. \end{aligned} \tag{4.1}$$

For the NCM chemistry, eqn. (4.1) is simplified by neglecting the impedance of the negative electrode. This assumption is validated by comparing the frequency responses as shown in Fig. 4.1. The positive electrode model closely matches the original SP model over the entire frequency range.

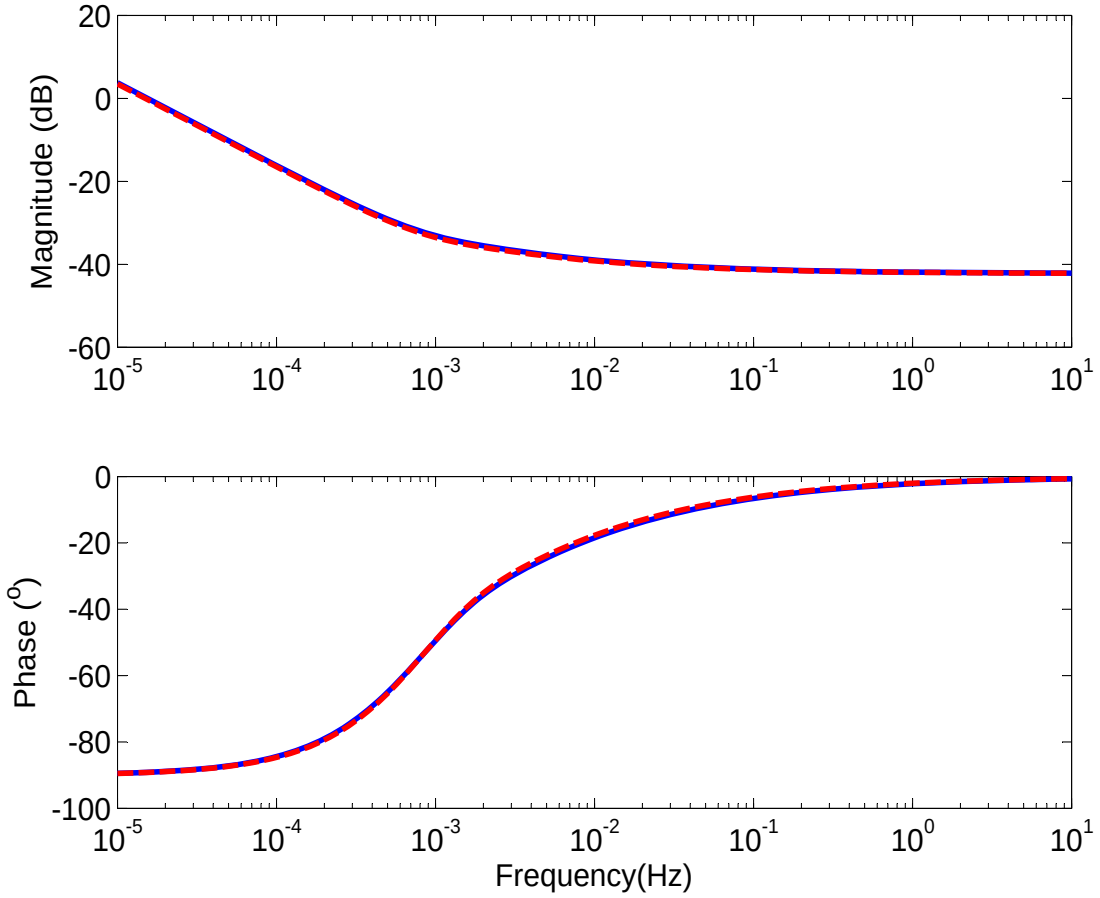

Figure 4.1. Impedance frequency response: SP model(blue-solid)and SP model with only positive electrode(red-dashed).

The simplified transfer function

$$Z(s) = \frac{R_T^+ s^3 + (21\mathcal{C}^+ + 189\frac{R_T^+}{\tau_D^+})s^2 + (1260\frac{\mathcal{C}^+}{\tau_D^+} + 3465\frac{R_T^+}{\tau_D^{+2}})s + 10395\frac{\mathcal{C}^+}{\tau_D^{+2}}}{s^3 + \frac{189}{\tau_D^+}s^2 + \frac{3465}{\tau_D^{+2}}s}. \quad (4.2)$$

However, for the LFP cells, the positive electrode has a flat open circuit potential for a wide range of operating state of charge as shown in fig. 4.2 and hence $\mathcal{C}^+ = \frac{\partial U}{\partial c_{s,e}}$ is almost zero. Therefore we can neglect the positive electrode dynamics from eqn. (4.1) and thereby the entire dynamics is solely contributed by the negative electrode. Hence, we get the third order transfer function as follows

$$Z(s) = \frac{R_T^- s^3 + (21\mathcal{C}^- + 189\frac{R_T^-}{\tau_D^-})s^2 + (1260\frac{\mathcal{C}^-}{\tau_D^-} + 3465\frac{R_T^-}{\tau_D^{-2}})s + 10395\frac{\mathcal{C}^-}{\tau_D^{-2}}}{s^3 + \frac{189}{\tau_D^-}s^2 + \frac{3465}{\tau_D^{-2}}s}. \quad (4.3)$$

The above transfer functions (4.2) and (4.3) depends only on the three composite parameters resistance $R_T^{+,-}$, capacity factor $\mathcal{C}^{+,-}$ and diffusion time $\tau_D^{+,-}$ (where superscript + is for NCM cells and - for LFP cells). Since the estimation of these parameters in both the chemistries involves the same procedure, we remove the +,- from the parameters for simplicity. These parameters can be estimated from experimental data and hence can be used to monitor the state of health of the battery.

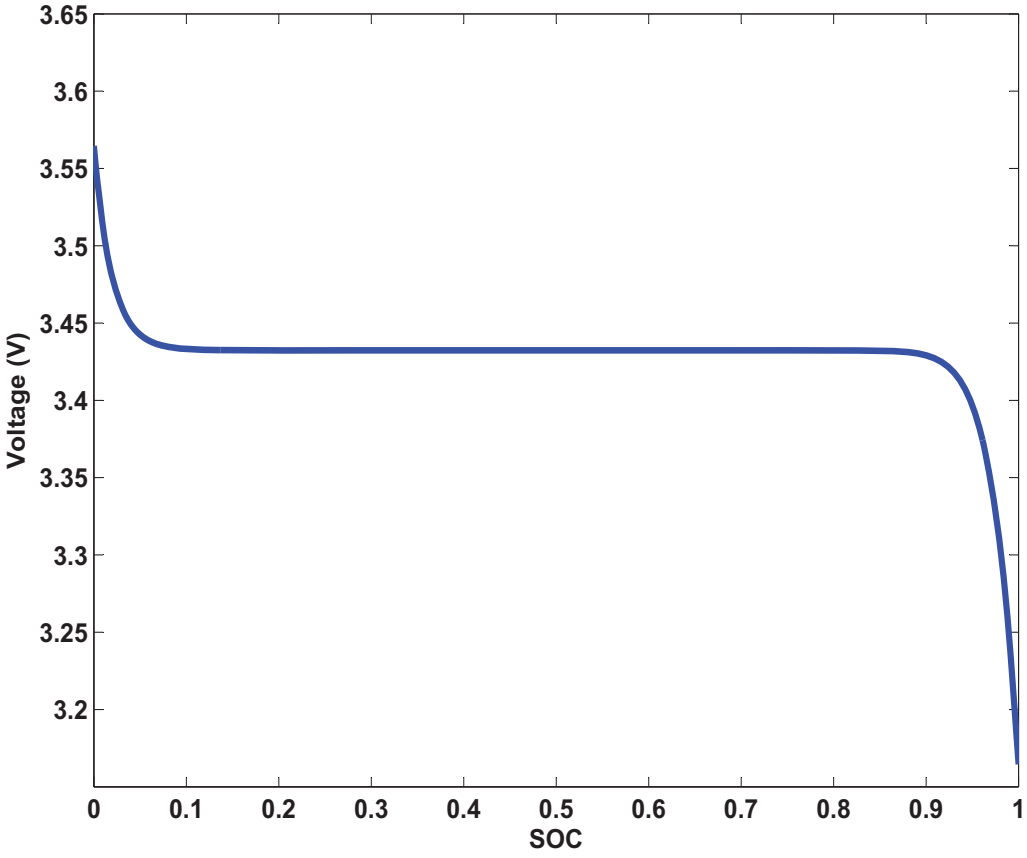

Figure 4.2. Open Circuit Potential of an LFP electrode.

4.2 Least Squares Parameter Estimation Algorithm

Using voltage measurements over a sufficiently long time and with persistently exciting current input, a least squares technique [52] can be used to identify the coefficients of the transfer functions (4.2) and (4.3) which has the form

$$\frac{V(s)}{I(s)} = \frac{b_3 s^3 + b_2 s^2 + b_1 s + b_0}{s^3 + a_2 s^2 + a_1 s} \tag{4.4}$$

The experimental current and voltage signals are passed through identical fourth order filters, represented in state space form by

$$\dot{\mathbf{w}}_1 = \Lambda \mathbf{w}_1 + \mathbf{b}_\lambda I(t), \tag{4.5}$$

$$\dot{\mathbf{w}}_2 = \Lambda \mathbf{w}_2 + \mathbf{b}_\lambda V(t), \tag{4.6}$$

where

$$\Lambda = \begin{bmatrix} 0 & 1 & 0 & 0 \\ 0 & 0 & 1 & 0 \\ 0 & 0 & 0 & 1 \\ -\lambda_0 & -\lambda_1 & -\lambda_2 & -\lambda_3 \end{bmatrix}, \quad \mathbf{b}_\lambda = \begin{bmatrix} 0 \\ \vdots \\ 1 \end{bmatrix}. \tag{4.7}$$

The coefficients $\lambda_0, \ldots, \lambda_3$ are calculated to place the poles of Λ in the left half of the complex plane at a desired filtering speed. The Laplace transform of Eqns. (4.5) and (4.6) produces

$$\frac{\mathbf{W}_1(s)}{I(s)} = \frac{1}{s^4 + \lambda_3 s^3 + \lambda_2 s^2 + \lambda_1 s^1 + \lambda_0} \begin{bmatrix} 1 \\ s \\ s^2 \\ s^3 \end{bmatrix}, \tag{4.8}$$

$$\frac{\mathbf{W}_2(s)}{V(s)} = \frac{1}{s^4 + \lambda_3 s^3 + \lambda_2 s^2 + \lambda_1 s^1 + \lambda_0} \begin{bmatrix} s \\ s^2 \end{bmatrix}, \tag{4.9}$$

The linear parametrization

$$\mathbf{b}^T\mathbf{W}_1(s) + \mathbf{a}^T\mathbf{W}_2(s) = \Theta^T\mathbf{W}(s), \tag{4.10}$$

where $\mathbf{b}^T = [b_0, b_1, b_2, b_3]$, $\mathbf{a}^T = [-a_1, -a_2]$, $\Theta^T = [\mathbf{b}^T, \mathbf{a}^T]$,
and $\mathbf{W}^T(s) = [\mathbf{W}_1^T(s), \mathbf{W}_2^T(s)]$ is expanded to obtain

$$\begin{aligned}\Theta^T\mathbf{W}(s) &= \frac{b_0 + b_1 s + b_2 s^2 + b_3 s^3}{s^4 + \lambda_3 s^3 + \lambda_2 s^2 + \lambda_1 s^1 + \lambda_0} I(s) \\ &\quad + \frac{-a_1 s - a_2 s^2}{s^4 + \lambda_3 s^3 + \lambda_2 s^2 + \lambda_1 s^1 + \lambda_0} V(s).\end{aligned} \tag{4.11}$$

Simplifying the above expression using the impedance transfer function in Eq. (4.4) we obtain

$$\Theta^T\mathbf{W}(s) = \frac{s^3}{s^4 + \lambda_3 s^3 + \lambda_2 s^2 + \lambda_1 s^1 + \lambda_0} V(s) = Z(s) \tag{4.12}$$

Therefore we have,

$$\hat{z}(t) = \hat{\Theta}^T\mathbf{w}(t), \tag{4.13}$$

where $\hat{\Theta}$ is the parameter estimate. The error is defined to be

$$e(t) = z(t) - \hat{z}(t) = z(t) - \hat{\Theta}^T\mathbf{w}(t). \tag{4.14}$$

The experimental voltage and current data is fed through the filters to produce

$$\mathbf{J} = \left[\mathbf{w}(0), \mathbf{w}(\Delta t), \ldots, \mathbf{w}((N_{eval} - 1)t)\right]. \tag{4.15}$$

where Δt is the sample time and N_{eval} is the total number of data points.

The least squares cost function

$$\text{CF} = |\mathbf{z} - \hat{\Theta}^T\mathbf{J}|^2, \tag{4.16}$$

so the $\hat{\Theta}$ that minimizes the CF is given by

$$\hat{\Theta}_{ls} = \left[\mathbf{J}\mathbf{J}^T\right]^{-1}\mathbf{J}\mathbf{z}. \tag{4.17}$$

In order to choose the poles of the filter, we write the characteristic equation of the filter in the form $(\tau s+1)^4$ where τ is the time constant of the filter. The filter time constant τ is chosen such that the estimated model captures the dynamics of the experimental voltage response accurately. The coefficients of the characteristic equation are given by

$$\lambda_0 = -1/\tau^4, \tag{4.18}$$
$$\lambda_1 = -4/\tau^3, \tag{4.19}$$
$$\lambda_2 = -6/\tau^2, \tag{4.20}$$
$$\lambda_3 = -4/\tau, \tag{4.21}$$
$$\tag{4.22}$$

The six parameters in $\hat{\Theta}_{ls}$ are the coefficients of the transfer function (4.4) that best-fit the experimental data in a least squares sense. The value of the filter time constant τ was chosen by a simple trial and error approach. If the model is accurate then the best-fit coefficients should correspond to a unique set of parameters R_T, $\mathcal{C}$, τ_D in the transfer functions (4.1) and (4.2). Equating transfer functions (4.4) and (4.1),(4.2) results in six nonlinear equations for the three unknown parameters. The best results were obtained by equating the two highest order coefficients in the numerator to produce $R_T = \hat{b_3}$ and $\mathcal{C} = \hat{b_2} - \hat{a_2}\hat{b_3}$ and the highest order coefficients in the denominator to produce $\tau_D = \frac{189}{\hat{a_2}}$.

4.2.1 Experimental Data for NCM and LFP cells

Seven commercial 3.1Ah NCM cells were cycled continuously at 5C-rate between 3.0 V and 4.2 V at 45^oC and four commercial 2.3Ah LFP cells were cycled continuously at 5C-rate between 2.0 V and 3.6 V at 50^oC on an Arbin BT-2000 battery cycler. The cycling of the seven NCM cells was terminated after 500, 1000, 2000,

3000, 4000, 5000 and 6000 cycles, respectively. For LFP cells, the cycling of the four cells was terminated after 3000 cycles. After cycling termination, the capacity, electrochemical impedance spectroscopy (EIS) data, and hybrid pulse power characterization(HPPC) [53] were measured. Figures 4.3 and 4.4 shows the measured capacity of these aged cells and a fresh cell. The pulse charge/discharge data from the HPPC test was obtained for each of the fresh and aged cells at 60% State of Charge (SOC), C-rates of 2C and 5C for different pulse durations (2s,10s and 30s), and at 25^{o}C. Figures 4.5 and 4.6 shows the input pulse train and the experimentally measured cell voltage response for a fresh NCM and LFP cell respectively.

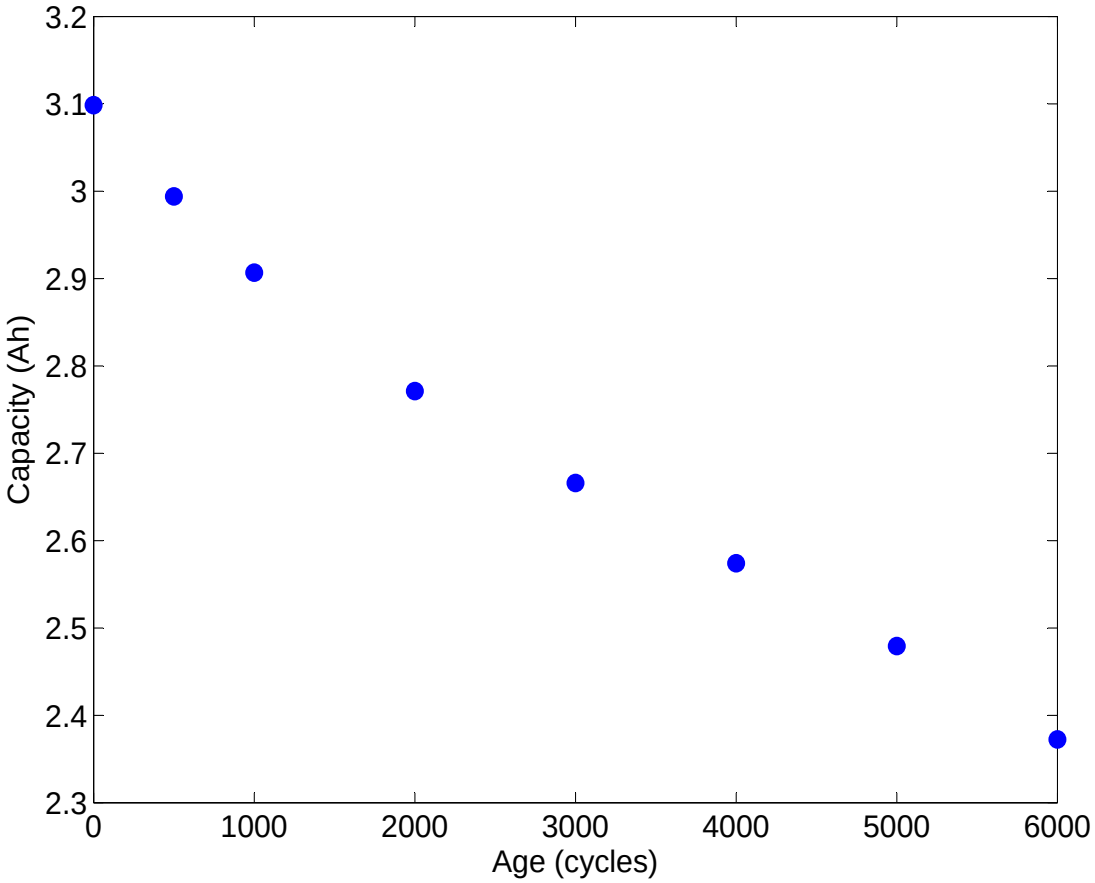

Figure 4.3. Experimentally measured capacity versus age for NCM cells

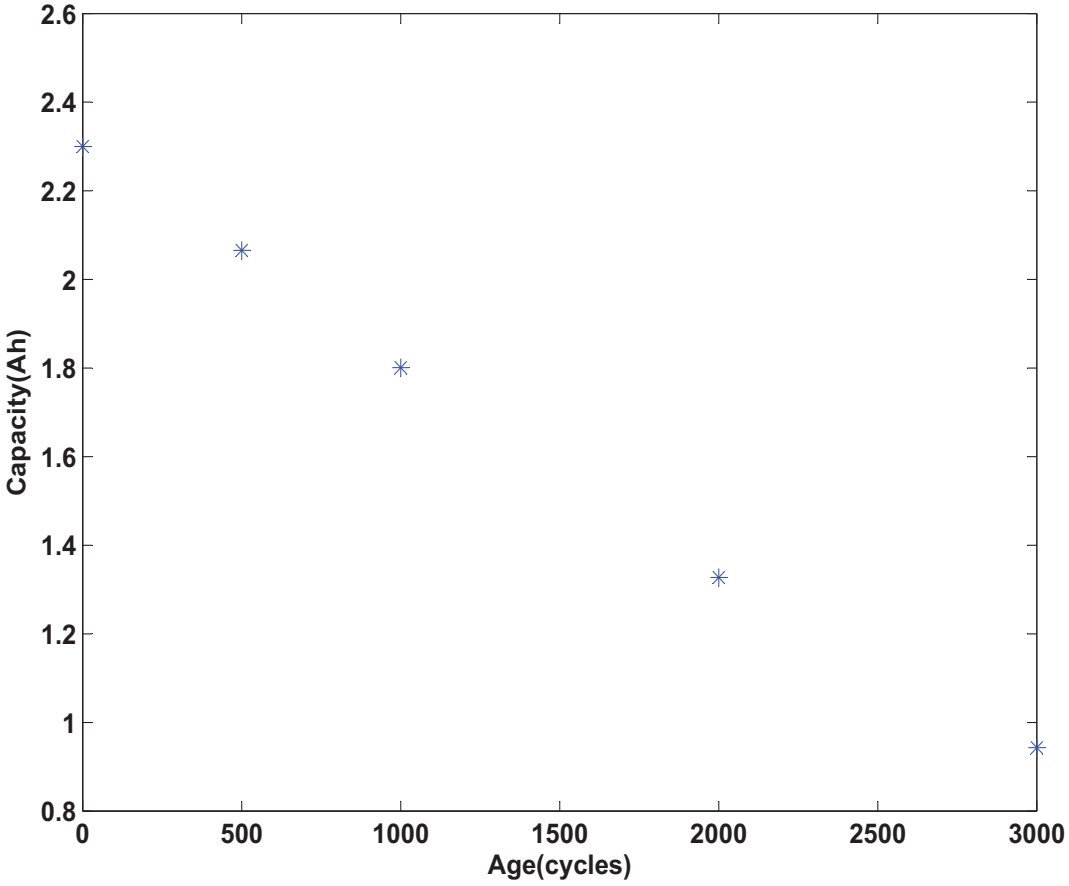

Figure 4.4. Experimentally measured capacity versus age for LFP cells

4.2.2 State of Health Estimation for NCM and LFP cells

The proposed methodology of SOH estimation from model parameter estimation is based on the following conditions:

- *The model parameters must be estimable from real-time measurements of voltage and current.* This requires that the model be sufficiently simple with few parameters and the voltage/current data must be sufficiently rich so that the parameters converge close to their actual values. The parameters R_T, $\mathcal{C}$, τ_D are estimated using the least squares technique from the experimental pulse current and voltage data, demonstrating that they satisfy this condition. Figures 4.5 and 4.6 shows the excellent match between the experimental and identified model voltage responses for a fresh cell using the estimated model

parameters. The overall response and the peaks/valleys match very well, including the high current and long duration 5C pulses. The SOC only deviates by 4% during these pulses, however, so the linearized OCV assumption applies.

- *The SOH or instantaneous capacity of the cell must be related to the model parameters by an invertible function.* The SOH as a function of parameter value must be invertible because the parameter will be estimated in real-time and the SOH calculated through this inverse function. The inverse function must be one-to-one so that a given parameter value only results in one possible SOH. Non-invertible functions that do not produce one-to-one results will have multiple possible SOH values for the same parameter value. This may be overcome by tracking the SOH over the life of the cell and using the value closest to the previous value. If the estimator ever "forgets" (e.g. power loss to microprocessor) the previous value, however, then it cannot be recovered. Parameters that vary monotonically with age are excellent candidates for SOH estimation because they are invertible and produce one-to-one inverse functions. The least squares technique is applied to all the eight NCM cells and five LFP cells. Figures 4.7 and 4.8 shows the estimated parameters as functions of age for NCM and LFP cells respectively.

- *The aging cycle test data must be representative of actual battery usage. The way a battery ages can depend on usage.* The current and temperature inputs must be representative of typical usage. The algorithm should then be validated against extreme cases to determine if the methodology holds up under those conditions. This would be a crucial step prior to adoption in practice.

The total resistance R_T includes the charge transfer resistance of the electrode and the contact resistance and the parameter estimate $\hat{R}_T$ increases significantly as the battery ages. Charge transfer resistance increase can be explained by the growth of a resistive SEI layer on the active particles of the electrode. Contact resistance generally increases with age due to contact loss between the electrode and the current collectors from corrosion.

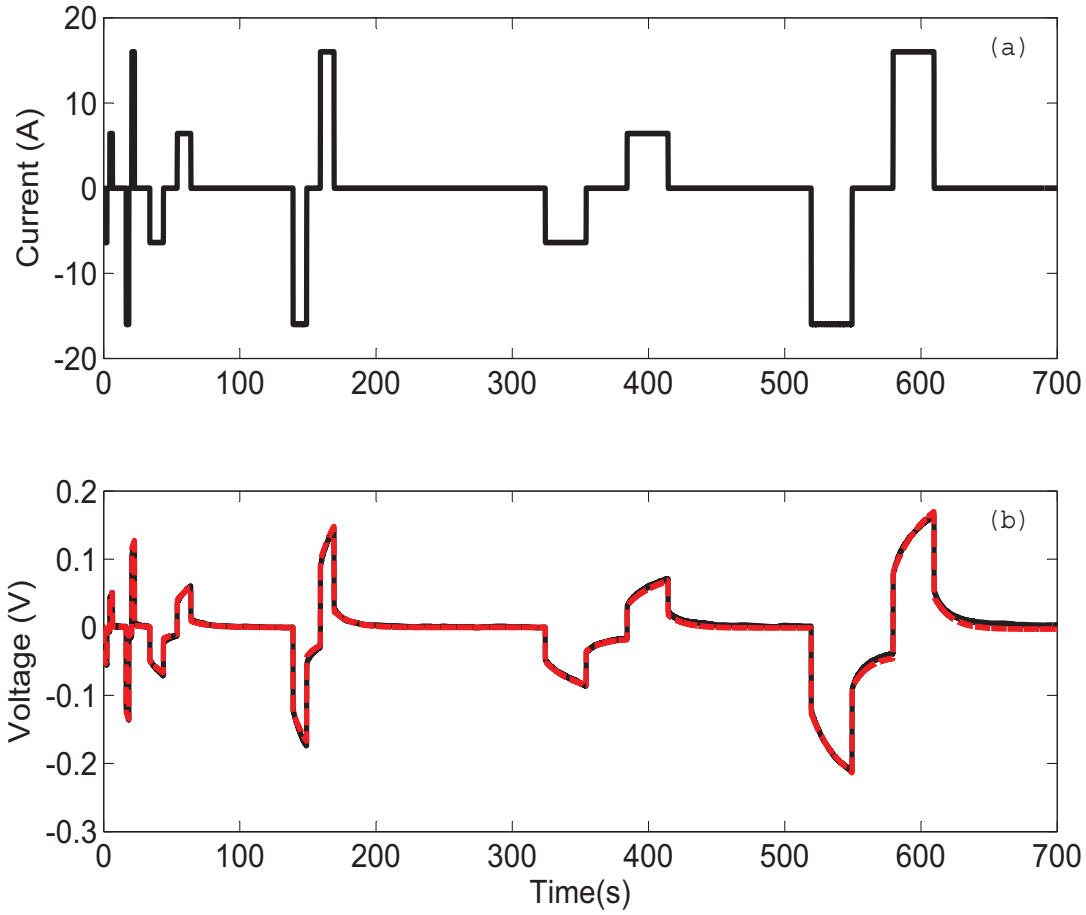

Figure 4.5. NCM - Pulse Charge/Discharge Response: (a) Input current and (b) Measured voltage (black-solid) and fitted model response (red-dashed)

For the NCM cells, the diffusion time parameter estimate τ_D^+ monotonically increases as the battery ages. The increase in the time taken for the Li^+ ions to diffuse can also be attributed to the growth of an SEI passivation layer on the active particles in the positive electrode which reduces the effective diffusion rate of Li^+. Whereas for the LFP cells even under the presence of an SEI layer on the surface of the negative electrode particle, the diffusion time parameter estimate monotonically decreases. This trend in the diffusion time for LFP cells can be attributed to the reduction in the crystallite size of the negative electrode. The reduction in crystallite size can be explained by the possibility of graphite exfoliation that could have occurred during the battery's life [29].

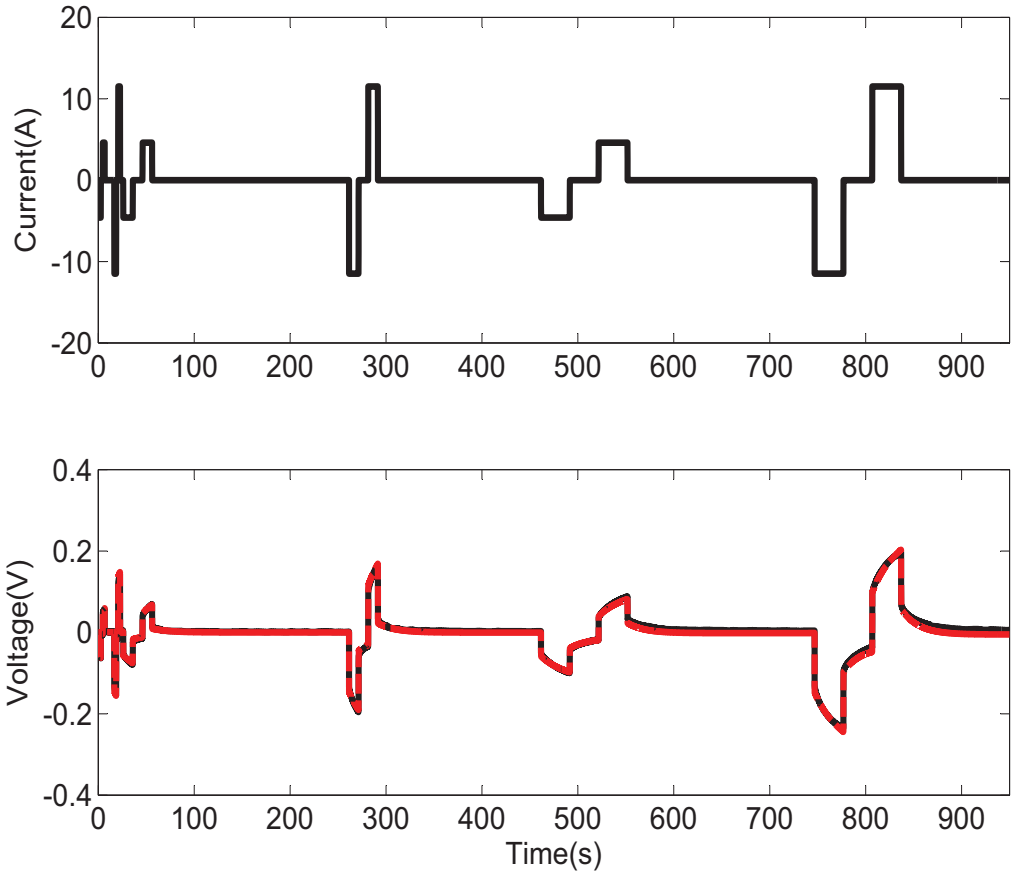

Figure 4.6. LFP - Pulse Charge/Discharge Response: (a) Input current and (b) Measured voltage (black-solid) and fitted model response (red-dashed)

Based on the empirical results in Fig. (4.7) and (4.8), three possible SOH estimates are

$$\hat{SOH}_{R_T}(t) = \frac{\hat{R}_T(t)}{\hat{R}_T(0)} \tag{4.23a}$$

$$\hat{SOH}_{\tau_D}(t) = \frac{\hat{\tau_D}(t)}{\hat{\tau_D}(0)} \tag{4.23b}$$

$$\hat{SOH}_{\mathcal{C}}(t) = \frac{\hat{\mathcal{C}}(t)}{\hat{\mathcal{C}}(0)} \tag{4.23c}$$

Figure (4.7) shows that the capacity factor estimate $\mathcal{C}^+$ for NCM cells rises slowly, reaching a maximum of 17 % at 4000 cycles. The estimate then decreases

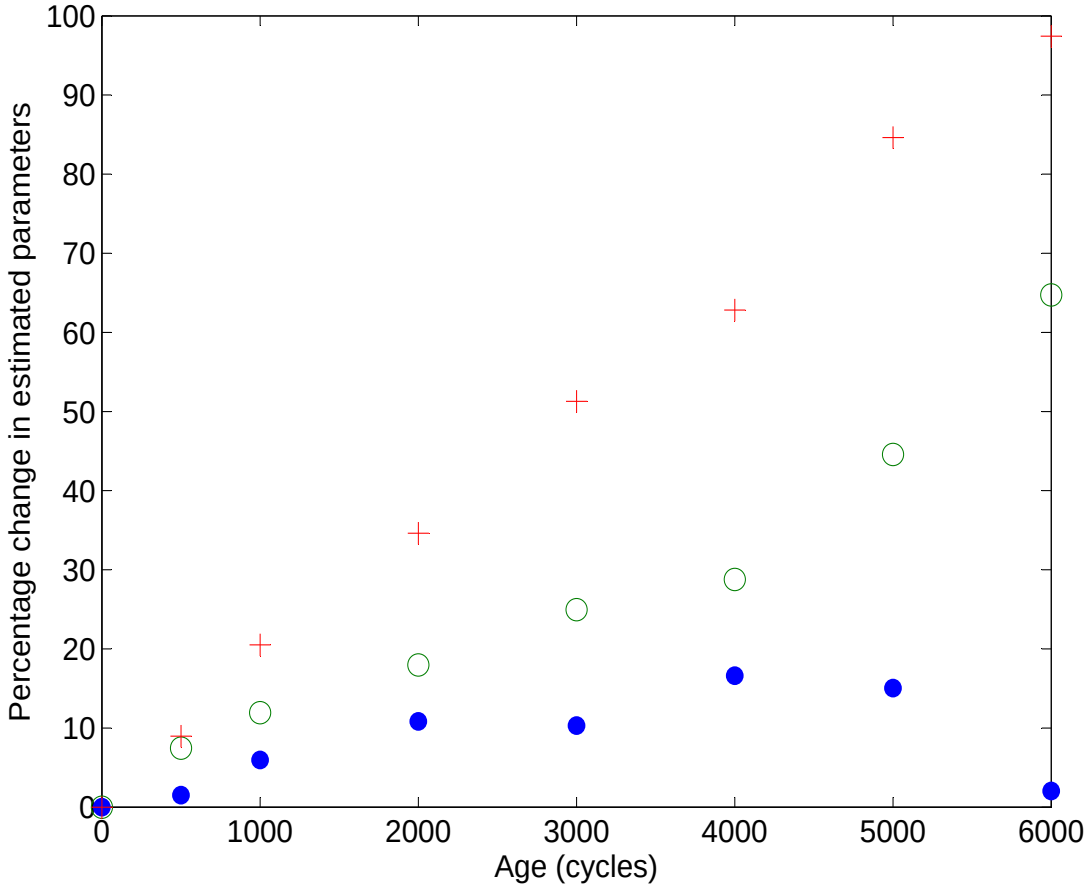

Figure 4.7. Estimated Resistance $(\hat{R}_T, +)$, diffusion time (τ_D^+, o), and capacity factor $(\mathcal{C}^+, \bullet)$ versus age for NCM cells.

almost back to its fresh cell value at end of life. This non-monotonic variation renders SOH estimation based on capacity factor impossible because the capacity factor estimate is the same at different ages as shown in Fig. (4.7). The capacity factor estimate cannot be inverted to infer the capacity because the inverse function is not one-to-one. However for the LFP cells as seen in fig. (4.8), the capacity factor shows a steady increase with age rendering it a good SOH indicator.

All three of the parameter estimates change in a fairly uniform way with little apparent random variations. This validates the modeling and least squares estimation approach and reflects the uniform degradation over time that is expected in the tested cells. The total resistance and diffusion time increase monotonically with age, making them excellent candidates for SOH estimation in both the

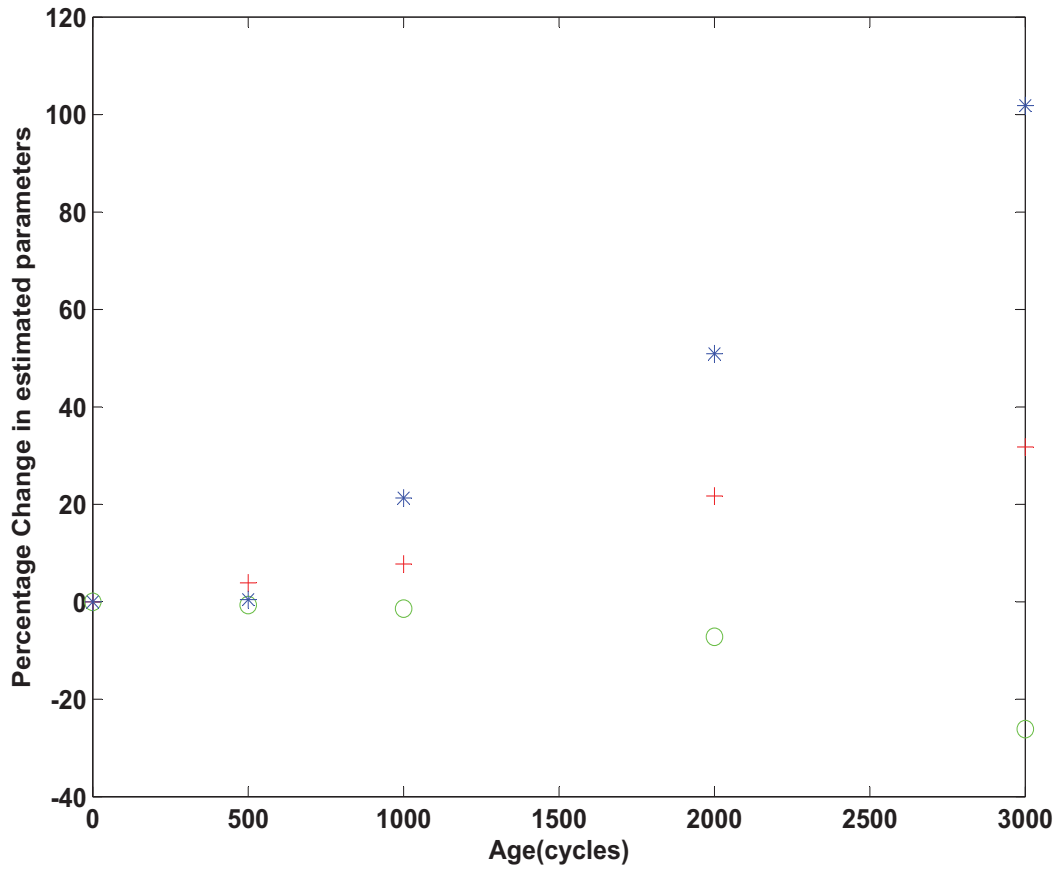

Figure 4.8. Estimated Resistance ($\hat{R}_T, +$), diffusion time (τ_D^-, o), and capacity factor ($\mathcal{C}^-, \bullet$) versus age for LFP cells.

chemistries. The capacity factor for LFP cells can be used as an SOH indicator due to its monotonic increase, however the capacity factor estimate curve for NCM cells is not invertible, because old and new cells give the same capacity factor estimate and hence will not make a good SOH indicator.

4.3 Recursive Parameter Estimation

The least squares approach provides a means of finding the best fit parameters for the SP model using a batch of current/voltage data and off-line processing. For real-time implementation onboard a vehicle, recursive parameter identification continually updates the parameter estimates using the all of the measured

the voltage and current data up to and including the current time instant. The estimation loop is run in the battery monitoring control software at a fixed sample rate and continually updates the estimates in real-time. This software is relatively simple and fast to execute, resulting in less burden on the battery monitoring microprocessor. This would be a crucial step prior to adoption in practice.

Fig. 4.9 shows the block diagram for the gradient based parameter estimator that is proposed for real-time parameter (and SOH via Eqs. 4.23) estimation. The objective is to estimate the parameter vector θ^T from the voltage and current data in real-time using a recursive algorithm that continually updates the parameter estimates as information becomes available. The parameter estimator include the input and output filters given by eqns. (4.5) and (4.6), respectively and two gradient update laws

$$\dot{\hat{b}} = \gamma_1 e(t) w_1(t) \tag{4.24}$$

$$\dot{\hat{a}} = \gamma_2 e(t) w_2(t) \tag{4.25}$$

that are integrated in real-time to produce the time-varying estimates of the numerator $\hat{\mathbf{b}}(\mathbf{t})$ and denominator $\hat{\mathbf{a}}(\mathbf{t})$ coefficients. The gradient update laws depend on the filtered current and voltage, the error

$$e(t) = z(t) - \left(\hat{\mathbf{b}} w_1(t) + \hat{\mathbf{a}} w_2(t)\right) \tag{4.26}$$

and the adaptation gain γ_1 and γ_2.

4.3.1 Recursive Parameter Identification from Experimental Data for fresh NCM cells

To demonstrate the functionality of the recursive parameter estimator, the fresh cell voltage and current data is processed in real-time as shown in Fig. 4.10. In this simulation, all of the coefficients are initialized to their least square, best fit values, except for the coefficients associated with the two SOH indicators, $\hat{R}_T^+(t)$ and $\tau_D^+(t)$, which are initialized to 5% of their actual values. The adaptation gains are adjusted to provide fast parameter convergence with minimal oscillation.

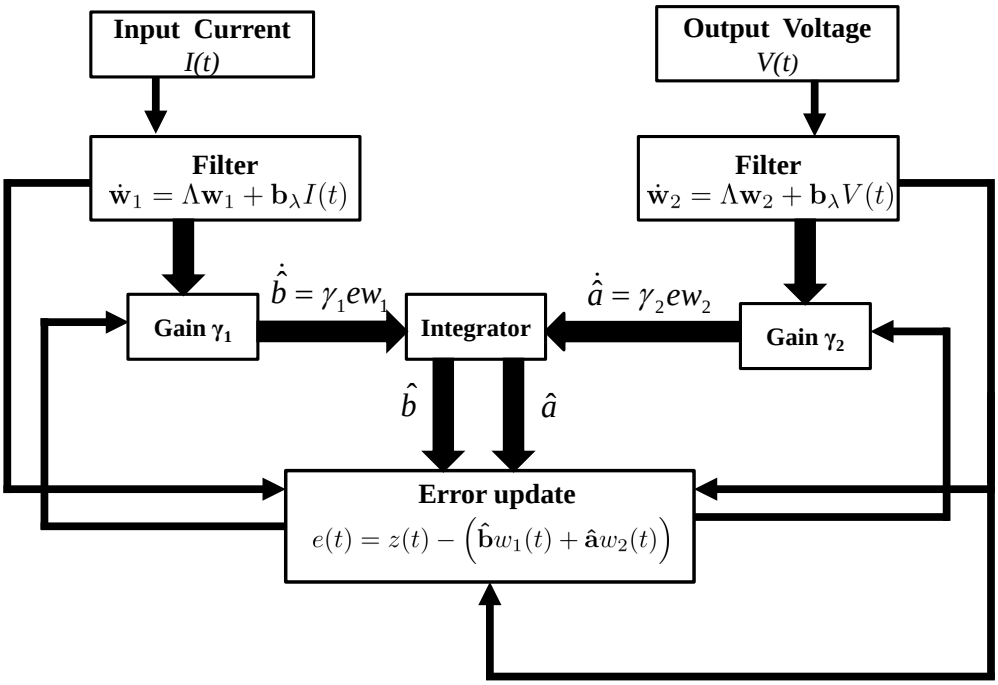

Figure 4.9. Recursive parameter estimator block diagram

The current excitation is sufficiently rich to ensure that the parameter estimates converge to within 99% of their least square, best fit values in less than 200 s.

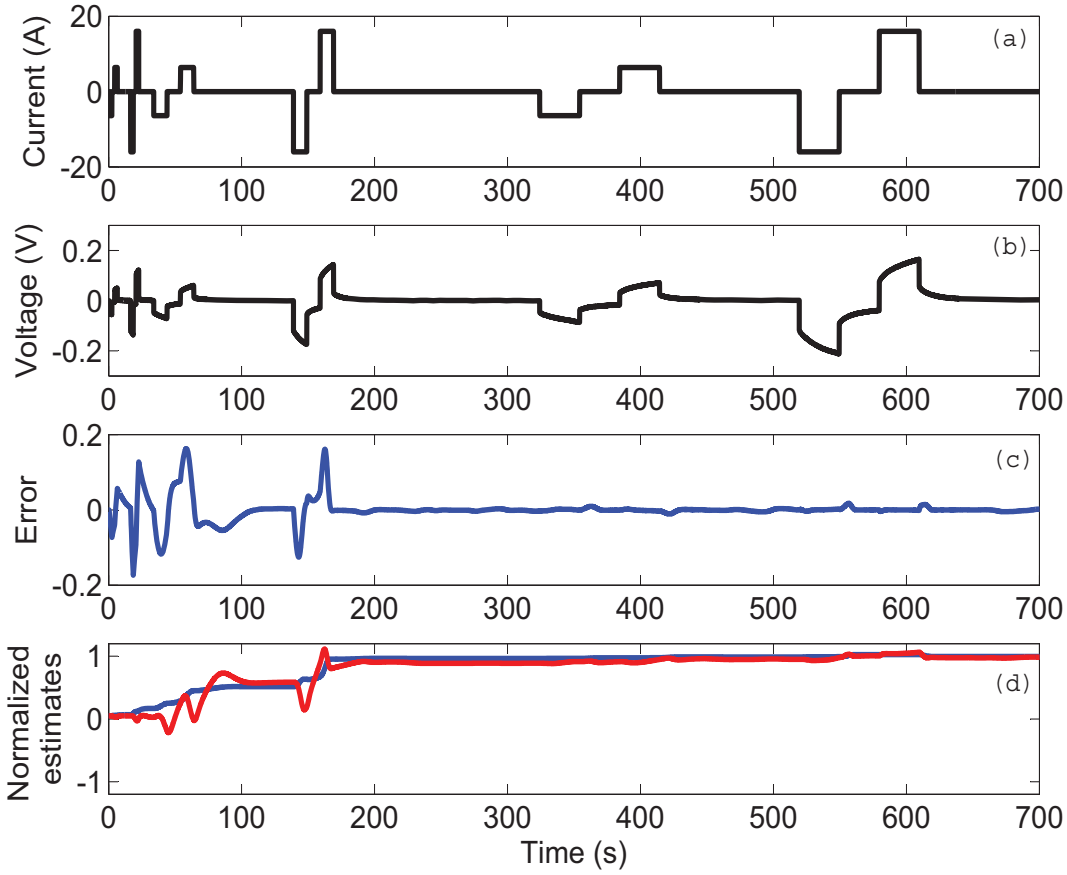

Figure 4.10. Gradient based recursive parameter estimation for a fresh NCM cell:(a) Current, (b) Voltage, (c) Error, (d) Normalized parameter estimates (Resistance (blue), Diffusion rate (Red))

Chapter 5

Development of a Control Oriented Degradation Model for a Lithium Iron Phosphate Battery

5.1 Introduction

This chapter presents the development of a reduced order aging model for a lithium ion battery by incorporating the solid electrolyte interphase (SEI) layer on the negative electrode particle surface. The SEI layer brings about a capacity fade in these cells by consuming cyclable lithium ions. The rate of degradation increases with increasing operating state of charge and with higher charging current. This degradation model is particularly well suited to explain the aging in lithium iron phosphate (LFP) batteries since the SEI layer formation in the negative electrode is the major factor responsible for degradation [29]. In other chemistries, the degradation in the positive electrode must also be considered to improve the model fidelity however in an LFP cell the positive electrode is extremely stable due to its olivine crystalline structure. The aging model is tuned and calibrated against experimental data.

5.2 Model Development

This model considers side reactions in the negative electrode leading to the formation of a SEI layer on the electrode surface to be the sole mechanism responsible for capacity fade and other mechanisms such as lithium plating is neglected. A very slow reduction process near the surface of the negative electrode leads to the formation of a passive film on the surface. The side reaction is expressed as

$$Solvent + 2Li^+ + 2e^- \rightarrow Product \tag{5.1}$$

The negative electrode used in an LFP battery is made up of a carbonaceous material, for *e.g* LiC_6. Ethylene Carbonate (EC) is a commonly used organic solvent and it undergoes reduction at the surface to form a mixture of organic and inorganic compounds. The SEI layer is made up of an inner thin compact inorganic layer and an outer porous organic layer. Due to the small thickness of the inner layer we assume the SEI layer to be a single phase uniformly covering the surface of the negative electrode particle. Moreover, the side reaction is assumed to be irreversible. We also assume that side reaction occurs only during the charging reaction.

In this model, we couple the aging equations with a nonlinear single particle model for the LFP cell. The model is valid for the entire range of state of charge and incorporates the nonlinear Butler Volmer kinetics as well.

In the single particle model we assume the total current density across the electrode domain to be uniform, hence we have the intercalation current density for the positive electrode to be equal to the total current density given by $j(t) = \frac{I(t)}{A\delta}$ where I is the applied current, A is the total surface of the cell, δ is the electrode thickness. However in the negative electrode the intercalation current density is given by the difference of the total current density and the side reaction current density.

$$j_-(t) = \frac{I(t)}{A\delta} - j_{sei}(t). \tag{5.2}$$

where $j_{sei}(t)$ is the side reaction current density.

From Chapter 4, the third order Padé approximated solid phase diffusion

impedance is given by

$$\frac{C_{s,e}(s)}{J(s)} = \frac{-21R_s^4s^2 - 1260R_s^2D_ss - 10395D_s^2}{a_sFR_s^5s^3 + 189a_sFR_s^3D_ss^3 + 3465a_sFR_sD_s^2s}. \tag{5.3}$$

The Butler Volmer equation that relates the intercalation current to the overpotential,

$$j_- = a_si_o\left\{\exp\left[\frac{\alpha_aF}{RT}\eta_-\right] - \exp\left[-\frac{\alpha_cF}{RT}\eta_-\right]\right\}. \tag{5.4}$$

This relation can be inverted to obtain

$$\eta_- = \frac{RT}{\alpha F}sinh^{-1}(\frac{j_-}{2a_si_0}). \tag{5.5}$$

The relationship between the overpotential in the negative electrode, the solid phase potential and the open circuit potential is given by

$$\eta_- = \phi_{s,-} - U(c_{s,e-}) - \frac{j}{a_s}R_{sei}. \tag{5.6}$$

The side reaction current density j_{sei} is driven by the side reaction overpotential and is described by the Tafel equation, analogous to the Butler Volmer equation,

$$j_{sei} = a_si_{o,s}\exp\left[\frac{\alpha_cF}{RT}\eta_{sei}\right]. \tag{5.7}$$

The side reaction overpotential is similarly related to the solid phase potential and the open circuit potential by

$$\eta_{sei} = \phi_s - U_{sei} - \frac{j}{a_s}R_{sei}. \tag{5.8}$$

Eqns. (5.8) and (5.6) can be subtracted to give

$$\eta_{sei} = U(c_{s,e-}) - U_{sei} - \eta_-. \tag{5.9}$$

The output voltage of the cell is given by

$$V = \phi_{s,+} - \phi_{s,-} - \frac{R_f}{A}I. \tag{5.10}$$

Eqn. (5.10) can be rewritten in terms of the overpotential and the open circuit potential to give the final form of the output voltage equation.

$$V = U(c_{s,e+}) - U(c_{s,e-}) + \frac{RT}{\alpha F} sinh^{-1}(\frac{j_+}{2a_{s+}i_0}) - \frac{RT}{\alpha F} sinh^{-1}(\frac{j_-}{2a_{s-}i_0}) - \frac{R_f}{A} I. \quad (5.11)$$

The increase in degradation parameters such as SEI film thickness δ_{sei} and its associated resistance R_{sei} can be calculated from

$$\frac{\partial \delta_{sei}}{\partial t} = -\frac{M_{sei}}{a_{s-}\rho_{sei}F} j_{sei}, \quad (5.12)$$

where M_{sei} and ρ_{sei} are the molar mass and density of the SEI film respectively, and

$$R_{sei} = R_{sei,0} + \frac{\delta_{sei}}{\kappa_{sei}}, \quad (5.13)$$

where $R_{sei,0}$ is the initial film resistance and κ_{sei} is the film conductivity.

The capacity loss is caused by the consumption of active Li^+ ions by the side reaction current and are related to each other by

$$\frac{\partial Q}{\partial t} = \int_0^{\delta_-} j_{sei} A dx \quad (5.14)$$

where Q is the capacity of the battery.

For any given input current cycle and a user initialized state of charge, the algorithm to compute the capacity fade at the end of the cycle can be described as follows.

At every time step i and for input current I(i) with a sample time of Δt

1. *Computation of Electrode Surface Concentration.*

   The surface concentration $c_{s,e}$ at the spherical electrode particle is calculated using the discrete state space form of the Pade approximated transfer function defined in eqn (5.3). The third order state space model for each electrode is given by

$$\begin{aligned} \text{x(i+1)} &= \text{Ax(i)} + \text{BI(i)} \quad (5.15) \\ c_{s,e}(i) &= \text{Cx(i)} \end{aligned}$$

where x is the state and A,B,C are the state space matrices. In the negative electrode the input current is updated at every time step by subtracting the current loss due to the SEI layer growth.

2. *Computation of Open Circuit Potential.*

   The electrode surface concentration obtained from the simulation of the state space model in the previous step is used to calculate the open circuit potential of the negative and positive electrode using the equations given in Table 5.1. The stoichiometry θ for the electrode is defined as $\theta = \frac{c_{s,e}}{c_{s,max}}$

3. *Computation of Exchange Current Density.*

   The exchange current density is computed using

$$i_0(i) = k(c_e)^{\alpha_a}(c_{s,max} - c_{s,e}(i))^{\alpha_a}(c_{s,e}(i))^{\alpha_c}. \tag{5.16}$$

4. *Computation of Negative Electrode Overpotential.*

   The overpotential in each electrode is calculated using the inverted Butler Volmer equation given by

$$\eta_-(i) = \frac{RT}{\alpha F} sinh^{-1}(\frac{j_-(i)}{2a_s i_0(i)}). \tag{5.17}$$

5. *Computation of Side Reaction Overpotential.*

   The side reaction overpotential is computed using

$$\eta_{sei}(i) = \eta_-(i) + U_-(c_{s,e}(i)) - U_{sei} \tag{5.18}$$

6. *Computation of Side Reaction Current Density.*

   The side reaction current density is computed using

$$j_{sei}(i) = a_s i_{o,s} \exp\left[\frac{\alpha_c F}{RT}\eta_{sei}(i)\right]. \tag{5.19}$$

7. *Computation of film resistance.*

The increase in film thickness and hence resistance is calculated using the discretized form of eqns. (5.12) and (5.13)

$$\delta_{sei}(i+1) = \delta_{sei}(i) - \frac{M_{sei}\Delta t}{a_{s-}\rho_{sei}F} j_{sei}(i) \tag{5.20}$$

$$R_{sei}(i+1) = R_{sei}(i) - \frac{M_{sei}\Delta t}{a_{s-}\rho_{sei}k_{sei}F} j_{sei}(i) \tag{5.21}$$

8. *Computation of Capacity Fade.*

   The capacity fade is calculated using the discretized form of eq. (5.14)

$$Q(i+1) = Q(i) + \frac{A\delta_{-}\Delta t j_{sei}(i)}{3600} \tag{5.22}$$

9. *Update negative electrode intercalation current density*

$$j_{-}(i+1) = \frac{I(i)}{A\delta_{-}} - j_{sei}(i) \tag{5.23}$$

5.3 Calibration and Validation of the Degradation Model

Most of the model parameters particularly the ones pertaining to the geometry of the cell such as electrode surface area and electrode thickness were taken from [26, 38]. We find that the negative electrode area is designed to be more than the positive electrode in order to avoid occurrence of lithium plating. The model was initially calibrated by tuning the stoichiometries of both the electrodes and simulating the model voltage response for a 0.1C discharge to match the experimental voltage response as shown in fig. 5.1.

The solid phase diffusion coefficient for the negative electrode was chosen to match the diffusion time estimated using the least squares approach described in chapter 4. The diffusion coefficient is calculated by $D_s = \frac{{R_s}^2}{\tau_d}$. The radius of the electrode particle was taken from [54]. The contact resistance was also calculated from the least square estimates of the total resistance. Table 5.1 lists the model parameters.

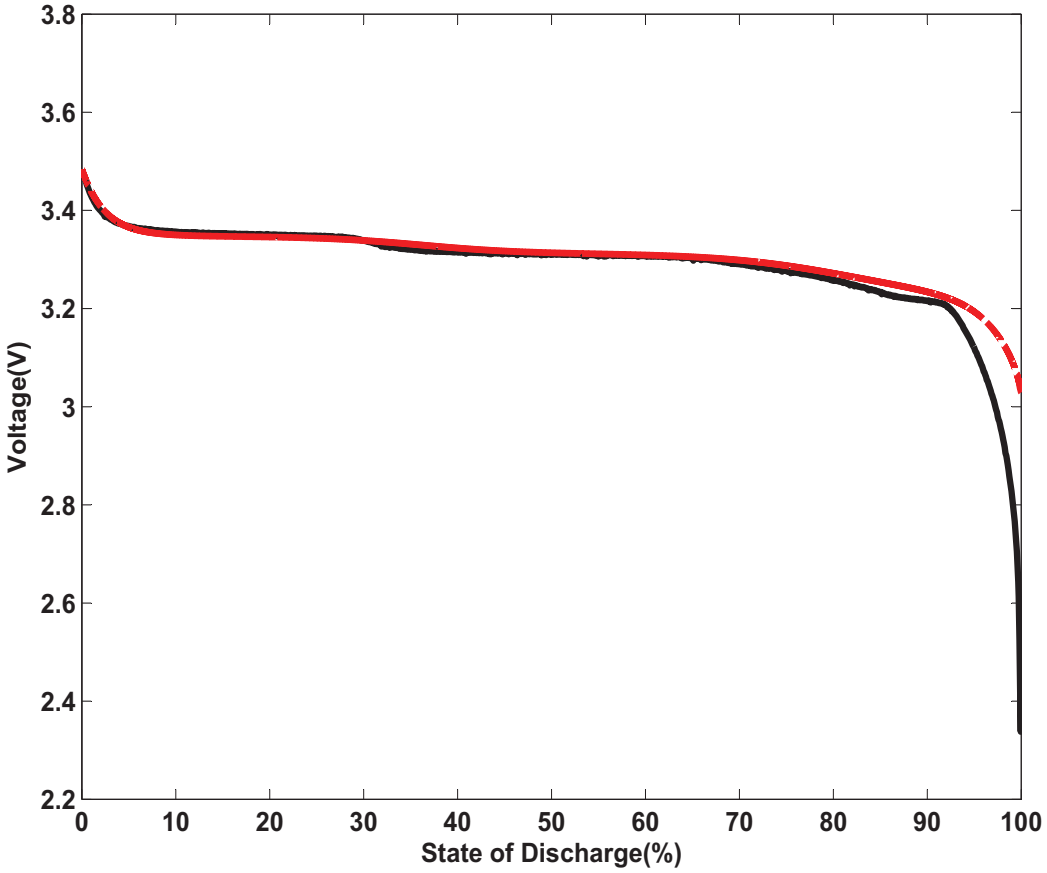

Figure 5.1. Discharge Response at 0.1C: Measured voltage (black-solid) and model response (red-dashed)

The cells were aged by continuously cycling it at 5C rate between 3.6V and 2.0V and at a temperature of 50 °C for accelerated aging. The model was calibrated against the measured capacity data of these aged cells. The degradation model is capable of predicting a linear drop in capacity fade and a linear increase in SEI film resistance. The model predicted capacity is compared to the experimentally measured capacity in Fig. 5.2. The primary tuning parameter is the exchange current density for the side reaction. The exchange current density term also incorporated the variation in temperature by the Arhennius relation. The exchange current density was tuned to match the experimental capacity loss at 500 cycles.

The increase in film resistance was also found to match the increase in resistance estimated using least squares. The conductivity of the SEI film was tuned to match

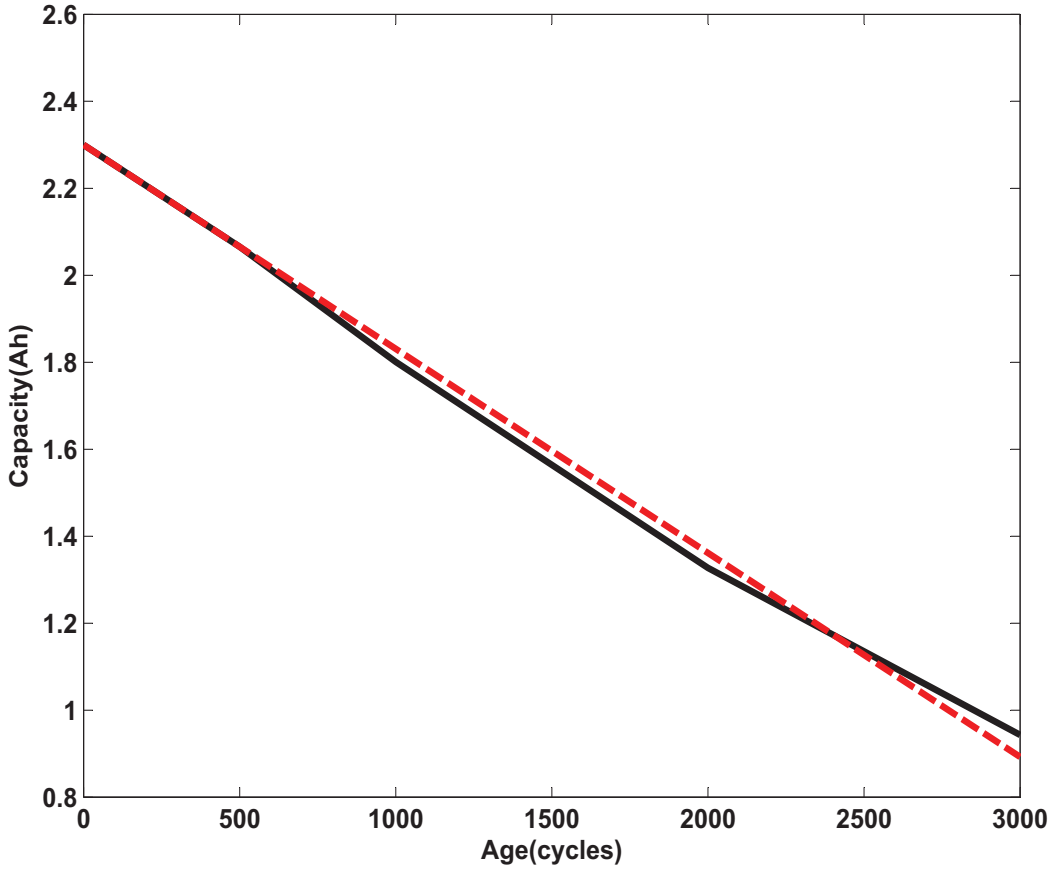

Figure 5.2. Measured capacity (black-solid) and model predicted capacity (red-dashed)

the resistance increase at the end of 500 cycles under the assumption that the initial rise in impedance can be solely contributed to the film thickness. The tuned value of the film conductivity was in close proximity to the value in [21]. From Fig. 5.3 we find that after around 1000 cycles the least square estimate of the resistance deviates from the model predicted SEI resistance possibly due to factors such as corrosion of current collector etc.

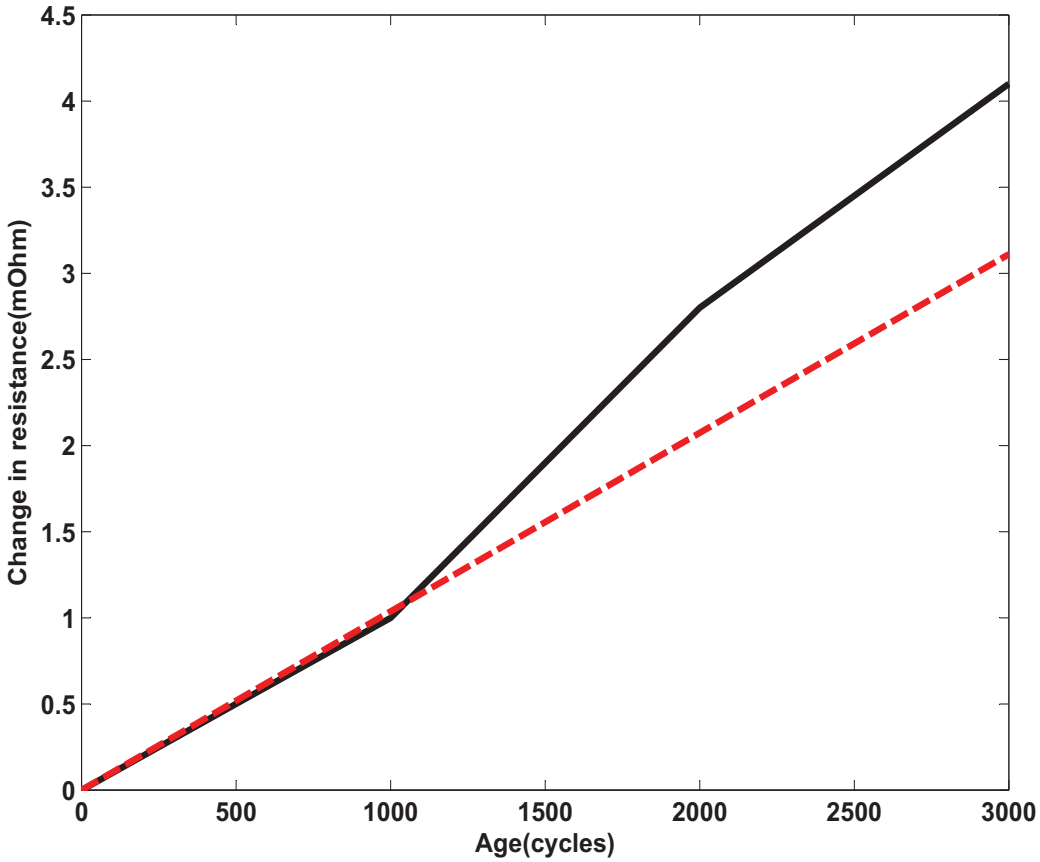

Figure 5.3. Estimated Resistance Increase (black-solid) and model predicted film resistance increase (red-dashed)

Table 5.1. Parameters for the LFP Cell Aging Model.

PARAMETER	**NEGATIVE**	**POSITIVE**
Thickness, δ $[cm]$	3.4×10^{-3}	7.0×10^{-3}
Particle radius, R_s $[cm]$	3.5×10^{-4}	3.65×10^{-6}
Active material volume fraction, ε_s	0.048	0.110
Solid Phase Diffusion Coefficient, D_s $[cm^2/s]$	3.29×10^{-11}	1.18×10^{-14}
Stoichiometry at 0% SOC, $x_{0\%}, y_{0\%}$	0.035	0.7767
Stoichiometry at 100% SOC, $x_{100\%}, y_{100\%}$	0.8685	0.035
Maximum Lithium Concentration $c_{s,max}$ $[mol/cm^3]$	31.370×10^{-3}	22.906×10^{-3}
Electrode Area, A $[cm^2]$	1755	01694
Open Circuit Potential [V]		
$U_+(y) = 3.4323 - 0.8428exp(-80.2493(1-y)^{1.3198}) - 3.2474 \times 10^{-6}exp(20.2645(1-y)^{3.8003}) + 3.2482 \times 10^{-6}exp(20.2646(1-y)^{3.7995})$		
$U_-(x) = 0.6379 + 0.5416exp(-305.5309x) + 0.044tanh(\frac{-x+0.1958}{0.1088}) - 0.1978tanh(\frac{x-1.0571}{0.0854}) - 0.6875tanh(\frac{x+0.0117}{0.0529}) - 0.0175tanh(\frac{x-0.5692}{0.0875})$		
Side Reaction Parameters		
Side Reaction Equilibrium Potential,U_{side} [V]	0.4	
Side Reaction Exchange Current Density, $i_{0,s}$ $[A/cm^2]$	2.595×10^{-11}	
SEI layer Molar Mass, M_{sei}[mol/kg]	0.162	
SEI layer density, ρ_{sei} $[kg/cm^3]$	1690×10^{-6}	
SEI Ionic Conductivity $[S/cm]$,k_{sei}	0.0600	
Activation Energy of Side Reaction [J/mol]	6×10^4	

Chapter 6

Conclusions and Future Work

6.1 Conclusions

Two linear control oriented models of a Li-ion battery based on the governing conservation and linearized Butler Volmer equations were developed. The frequency and time domain responses of these reduced order models match well with experimental results for a 3.1Ah NCM battery. The reduced order (RO) model captures the dynamics of internal variables such as electrolyte and electrode surface concentration distributions. The single particle (SP) model uses a 5^{th} order Padé approximation and can be realized by an equivalent circuit where the resistances and capacitances are explicitly related to the physical parameters of the battery

A third order, single particle, single electrode model of Li-ion cells enables the development of least square and recursive parameter estimators. Least square estimates of the composite parameters of total resistance and diffusion time are shown to increase monotonically with age of commercial NCM cells that have been charged/discharged at 5C at 45^oC for up to 6000 cycles. These results are consistent with the growth of an SEI layer that increases resistance and limits the diffusion rate of aged cells. With sufficiently rich current excitation, the total resistance and diffusion time estimates converge to within 99% of their best fit values in 200 s using a gradient parameter update law in real time. The total resistance and diffusion time estimates provide two independent measures of NCM battery SOH that can be calculated in real time, on-board a vehicle. A similar approach was implemented for lithium iron phosphate cells where a third order

single particle model was developed by including only the dynamics of the negative electrode and neglecting the positive electrode due to the flat open circuit potential of the LFP electrode. The least square estimates of the total resistance and the capacity factor are shown to increase monotonically with age of commercial LFP cells that have been charged/discharged at 5C at 50^oC for up to 3000 cycles. The increase in resistance can be attributed to the growth of the SEI layer on the surface of the negative electrode particle and corrosion of current collectors. However the diffusion time in the negative electrode was found to decrease monotonically which can be explained by the reduction in crystallite size due to graphite exfoliation. The steady increase/decrease in these three parameters render all of them to be excellent SOH indicators for an LFP cell.

Finally, a control oriented degradation model was developed by incorporating the aging mechanism of SEI layer growth in the negative electrode with a nonlinear single particle model. This is the major degradation mechanism in LFP cells since its olivine structured positive electrode does not age appreciably due to its extreme stability. The model predicts the experimentally measured capacity loss and increase in film resistance.

6.2 Future Work

6.2.1 Development of Better Aging Models and Validation

It is extremely important to develop high fidelity control oriented aging models by incorporating different aging mechanisms responsible for impedance rise and capacity fade. Perkins *et al* [55] developed a control oriented reduced order model of lithium deposition on overcharge (lithium plating). Overcharging leading to lithium plating causes an irreversible loss of lithium ions and hence a severe drop in capacity. Highly accurate models can also be developed by considering the side reactions and aging mechanisms in the positive electrode as well. Researchers [43]have studied the presence of a passive layer that is formed on the positive electrode particle surface which can cause an increase in the cell impedance. A more reliable control oriented aging model can be developed by incorporating the degradation mechanisms in both the positive and negative electrodes.

Another major failure mechanism in lithium ion batteries is the coupled mechanical chemical degradation of electrodes [56, 57]. Irreversible capacity loss occurs due to diffusion induced stresses (DISs) that cause pre-existing cracks on the electrode surfaces to grow gradually upon cycling, leading to the growth of SEI on the newly exposed electrode surfaces. It would be challenging and interesting to model the crack propagation due to diffusion induced stress in a control oriented framework. These aging models must be validated against experimental data and the parameters must be estimated and identified accurately.

6.2.2 Identification of Minimally Degrading Current Profiles

A high fidelity and validated degradation model can be used to identify current profiles that induces minimum degradation via optimal control algorithms. For example, using a single particle physics based capacity fade model and dynamic optimization, Rahimian *et al* [58] found that the life of a lithium ion cell can be maximized by applying different charge rates during cycling.

6.2.3 Inclusion of the Effect of Temperature

It is extremely important to incorporate the effect of temperature and the corresponding variation in the model parameters to develop an accurate thermal model in a control oriented manner. First principles based electro-thermal models have been developed by incorporating the heat generation and the temperature dependence of the various transport, kinetic and mass transfer parameters [59, 60, 61]. Guo *et al* [62] extended the single particle electrochemical model developed by Santhanagopalan *et al* [63] to include the energy balance as well as the temperature dependence of the solid phase diffusion coefficient of the lithium in the intercalation particles, the electrochemical reaction rate constants, and the open circuit potentials of the positive and negative electrodes. Temperature also plays a critical role in aging. At high temperatures the battery ages faster along with an increase in resistance [64]. In the future, a high fidelity control oriented thermo-coupled aging model will be an excellent and very useful tool for the electrified vehicle and battery communities.

Bibliography

[1] Lowe, M., S. Tokuoka, and T. Trigg *Lithium-ion Batteries for Electric Vehicles: The US Value Chain*, *Tech. rep.*

[2] Padhi, A. K., K. S. Nanjundaswamy, and J. B. Goodenough (1997) "Phospho-olivines as Positive-Electrode Materials for Rechargeable Lithium Batteries," *Journal of The Electrochemical Society*, **144**(4), pp. 1188–1194.

[3] Yamada, A., M. Hosoya, S.-C. Chung, Y. Kudo, K. Hinokuma, K.-Y. Liu, and Y. Nishi (2003) "Olivine-type cathodes: Achievements and problems," *Journal of Power Sources*, **119121**(0), pp. 232 – 238.

[4] MacNeil, D., Z. Lu, Z. Chen, and J. Dahn (2002) "A comparison of the electrode/electrolyte reaction at elevated temperatures for various Li-ion battery cathodes," *Journal of Power Sources*, **108**(12), pp. 8 – 14.

[5] Plett, G. L. (2004) "Extended Kalman filtering for battery management systems of LiPB-based HEV battery packs: Part 1. Background," *Journal of Power Sources*, **134**(2), p. 252261.

[6] ——— (2004) "Extended Kalman filtering for battery management systems of LiPB-based HEV battery packs: Part 2. Modeling and identification," *Journal of Power Sources*, **134**(2), p. 262276.

[7] ——— (2004) "Extended Kalman filtering for battery management systems of LiPB-based HEV battery packs: Part 3.State and parameter estimation," *Journal of Power Sources*, **134**(2), p. 277292.

[8] Dong, T. K., A. Kirchev, F. Mattera, and Y. Bultel (2010) "Modeling of Lithium Iron Phosphate Batteries by an Equivalent Electrical Circuit: Method of Model Parameterization and Simulation," *ECS Transactions*, **25**(35), pp. 131–138.

[9] Dong, T. K., A. Kirchev, F. Mattera, J. Kowal, and Y. Bultel (2011) "Dynamic Modeling of Li-Ion Batteries Using an Equivalent Electrical Circuit," *Journal of The Electrochemical Society*, **158**(3), pp. A326–A336.

[10] Verbrugge, M. W. and R. S. Conell (2002) "Electrochemical and thermal characterization of battery modules commensurate with electric vehicle integration," *Journal of The Electrochemical Society*, **149**(1), pp. A45–A53.

[11] ——— (2007) "Electrochemical characterization of high-power lithium ion batteries using triangular voltage and current excitation sources," *Journal of Power Sources*, **174**(1), pp. 2–8.

[12] Chen, M. and G. A. Rincn-Mora (2006) "Accurate electrical battery model capable of predicting runtime and IV performance," *IEEE Transactions on Energy Conversion*, **21**(2), pp. 504–511.

[13] Schweighofer, B., K. M. Raab, and G. Brasseur (2003) "Modeling of high power automotive batteries by the use of an automated test system," *IEEE Transactions on Instrumentation and Measurement*, **52**(4), pp. 1087–1091.

[14] Moss, P. L., G. Au, E. J. Plichta, and J. P. Zheng (2008) "An Electrical Circuit for Modeling the Dynamic Response of Li-Ion Polymer Batteries," *Journal of The Electrochemical Society*, **155**(12), pp. A986–A994.

[15] Hu, X., S. Li, and H. Peng (2012) "A comparative study of equivalent circuit models for Li-ion batteries," *Journal of Power Sources*, **198**, pp. 359–367.

[16] Hu, Y., S. Yurkovich, Y. Guezennec, and B. J. Yurkovich (2011) "Electro-thermal battery model identification for automotive applications," *Journal of Power Sources*, **196**, pp. 449–457.

[17] Doyle, M., T. Fuller, and J. Newman (1993) "Modeling of galvanostatic charge and discharge of the lithium/polymer/insertion cell," *Journal of the Electrochemical Society*, **140**, pp. 1526–33.

[18] Fuller, T., M. Doyle, and J. Newman (1994) "Simulation and optimization of the dual lithium ion insertion cell," *Journal of the Electrochemical Society*, **141**, pp. 1–10.

[19] Smith, K. A., C. D. Rahn, and C.-Y. Wang (2007) "Control oriented 1D electrochemical model of lithium ion battery," *Energy Conversion and Management*, **48**, pp. 2565–2578.

[20] ——— (2008) "Model Order Reduction of 1-D diffusion systems via residue grouping," *ASME Journal of Dynamic Systems, Measurement, and Control*, **130**(5), pp. 011012–1–011012–8.

[21] Ramadass, P., B. Haran, P. M. Gomadam, R. White, and B. N. Popov (2004) "Development of First Principles Capacity Fade Model for Li-Ion Cells," *Journal of The Electrochemical Society*, **151**(2), pp. A196–A203.

[22] Gomadam, P. M., J. W. Weidner, R. A. Dougal, and R. E. White (2002) "Mathematical modeling of lithium-ion and nickel battery systems," *Journal of Power Sources*, **110**, pp. 267–284.

[23] Malik, R., A. Abdellahi, and G. Ceder (2013) "A Critical Review of the Li Insertion Mechanisms in LiFePO4 Electrodes," *Journal of The Electrochemical Society*, **160**(5), pp. A3179–A3197.

[24] Srinivasan, V. and J. Newman (2004) "Discharge Model for the Lithium Iron-Phosphate Electrode," *Journal of The Electrochemical Society*, **151**(10), pp. A1517–A1529.

[25] Safari, M. and C. Delacourt (2011) "Mathematical Modeling of Lithium Iron Phosphate Electrode: Galvanostatic Charge/Discharge and Path Dependence," *Journal of The Electrochemical Society*, **158**(2), pp. A63–A73.

[26] ——— (2011) "Modeling of a Commercial Graphite/LiFePO4 Cell," *Journal of The Electrochemical Society*, **158**(5), pp. A562–A571.

[27] Prada, E., D. Di Domenico, Y. Creff, J. Bernard, V. Sauvant-Moynot, and F. Huet (2012) "Simplified Electrochemical and Thermal Model of LiFePO4-Graphite Li-Ion Batteries for Fast Charge Applications," *Journal of The Electrochemical Society*, **159**(9), pp. A1508–A1519.

[28] Marcicki, J., M. Canova, A. T. Conlisk, and G. Rizzoni (2013) "Design and parametrization analysis of a reduced-order electrochemical model of graphite/LiFePO4 cells for SOC/SOH estimation," *Journal of Power Sources*, **237**, pp. 310 – 324.

[29] Liu, P., J. Wang, J. Hicks-Garner, E. Sherman, S. Soukiazian, M. Verbrugge, H. Tataria, J. Musser, and P. Finamore (2010) "Aging Mechanisms of LiFePO4 Batteries Deduced by Electrochemical and Structural Analyses," *Journal of The Electrochemical Society*, **157**(4), pp. A499–A507.

[30] Vetter, J., P. Novák, M. Wagner, C. Veit, K.-C. Moller, J. Besenhard, M. Winter, M. Wohlfahrt-Mehrens, C. Vogler, and A. Hammouche (2005) "Ageing mechanisms in lithium-ion batteries," *Journal of Power Sources*, **147**, pp. 269 – 281.

[31] Broussely, M., S. Herreyre, P. Biensan, P. Kasztejna, K. Nechev, and R. Staniewicz (2001) "Aging mechanism in Li ion cells and calendar life predictions," *Journal of Power Sources*, **9798**(0), pp. 13 – 21.

[32] Sarre, G., P. Blanchard, and M. Broussely (2004) "Aging of lithium-ion batteries," *Journal of Power Sources*, **127**(12), pp. 65 – 71.

[33] Broussely, M., P. Biensan, F. Bonhomme, P. Blanchard, S. Herreyre, K. Nechev, and R. Staniewicz (2005) "Main aging mechanisms in Li ion batteries," *Journal of Power Sources*, **146**(12), pp. 90 – 96.

[34] Christensen, J. and J. Newman (2004) "A Mathematical Model for the Lithium-Ion Negative Electrode Solid Electrolyte Interphase," *Journal of The Electrochemical Society*, **151**(11), pp. A1977–A1988.

[35] Ning, G. and B. N. Popov (2004) "Cycle Life Modeling of Lithium-Ion Batteries," *Journal of The Electrochemical Society*, **151**(10), pp. A1584–A1591.

[36] Ning, G., R. E. White, and B. N. Popov (2006) "A generalized cycle life model of rechargeable Li-ion batteries," *Electrochimica Acta*, **51**(10), pp. 2012 – 2022.

[37] Randall, A. V., R. D. Perkins, X. Zhang, and G. L. Plett (2012) "Controls oriented reduced order modeling of solid-electrolyte interphase layer growth," *Journal of Power Sources*, **209**, pp. 282 – 288.

[38] Prada, E., D. Di Domenico, Y. Creff, J. Bernard, V. Sauvant-Moynot, and F. Huet (2013) "A Simplified Electrochemical and Thermal Aging Model of LiFePO4-Graphite Li-ion Batteries: Power and Capacity Fade Simulations," *Journal of The Electrochemical Society*, **160**(4), pp. A616–A628.

[39] Zhang, D., B. Haran, A. Durairajan, R. White, Y. Podrazhansky, and B. Popov (2000) "Studies on capacity fade of lithium-ion batteries," *Journal of Power Sources*, **91**(2), pp. 122 – 129.

[40] Stamps, A. T., C. E. Holland, R. E. White, and E. P. Gatzke (2005) "Analysis of capacity fade in a lithium ion battery," *Journal of Power Sources*, **150**(0), pp. 229 – 239.

[41] Ramadass, P., B. Haran, R. White, and B. N. Popov (2003) "Mathematical modeling of the capacity fade of Li-ion cells," *Journal of Power Sources*, **123**(2), pp. 230 – 240.

[42] Schmidt, A. P., M. Bitzer, A. W. Imre, and L. Guzzella (2010) "Model-based distinction and quantification of capacity loss and rate capability fade in Li-ion batteries," *Journal of Power Sources*, **195**, p. 76347638.

[43] Zhang, Y. and C.-Y. Wang (2009) "Cycle-Life Characterization of Automotive Lithium-Ion Batteries with $LiNiO_2$ Cathode," *Journal of The Electrochemical Society*, **156**(7), pp. A527–A535.

[44] Remmlinger, J., M. Buchholz, M. Meiler, P. Bernreuter, and K. Dietmayer (2011) "State-of-health monitoring of lithium-ion batteries in electric vehicles by on-board internal resistance estimation," *Journal of Power Sources*, **196**(12), pp. 5357 – 5363.

[45] Kim, J. and B. Cho (2011) "State-of-Charge Estimation and State-of-Health Prediction of a Li-Ion Degraded Battery Based on an EKF Combined With a Per-Unit System," *Vehicular Technology, IEEE Transactions on*, **60**(9), pp. 4249 –4260.

[46] Haifeng, D., W. Xuezhe, and S. Zechang (2009) "A new SOH prediction concept for the power lithium-ion battery used on HEVs," in *Vehicle Power and Propulsion Conference, 2009. VPPC '09. IEEE*, pp. 1649 –1653.

[47] Troltzsch, U., O. Kanoun, and H.-R. Trankler (2006) "Characterizing aging effects of lithium ion batteries by impedance spectroscopy," *Electrochimica Acta*, **51**, pp. 1664–1672.

[48] Kim, I.-S. (2010) "A Technique for Estimating the State of Health of Lithium Batteries Through a Dual-Sliding-Mode Observer," *Power Electronics, IEEE Transactions on*, **25**(4), pp. 1013 –1022.

[49] Jacobsen, T. and G. West (1995) "Diffusion impedance in planar, cylindrical and spherical geometry," *Electrochimica Acta*, **40**(2), pp. 255–262.

[50] Forman, J. C., S. Bashash, J. L. Stein, and H. K. Fathy (2011) "Reduction of an Electrochemistry-Based Li-Ion Battery Model via Quasi-Linearization and Pad Approximation," *Journal of The Electrochemical Society*, **158**(2), pp. A93–A101.

[51] Shi, Y., G. Prasad, Z. Shen, and C. D. Rahn "Discretization Methods for Battery Systems Modeling," in *Proceedings of the American Control Conference 2011, San Francisco, CA*, San Francisco, CA.

[52] Sastry, S. and M. Bodson (1994) *Adaptive Control-Stability,Convergence and Robustness*, Prentice-Hall.

[53] Zhang, Y., C.-Y. Wang, and X. Tang (2011) "Cycling degradation of an automotive LiFePO4 lithium-ion battery," *Journal of Power Sources*, **196**(3), pp. 1513 – 1520.

[54] Safari, M. and C. Delacourt (2011) "Aging of a Commercial Graphite/LiFePO4 Cell," *Journal of The Electrochemical Society*, **158**(10), pp. A1123–A1135.

[55] Perkins, R. D., A. V. Randall, X. Zhang, and G. L. Plett (2012) "Controls oriented reduced order modeling of lithium deposition on overcharge," *Journal of Power Sources*, **209**(0), pp. 318 – 325.

[56] Deshpande, R., M. Verbrugge, Y.-T. Cheng, J. Wang, and P. Liu (2012) "Battery Cycle Life Prediction with Coupled Chemical Degradation and Fatigue Mechanics," *Journal of The Electrochemical Society*, **159**(10), pp. A1730–A1738.

[57] Narayanrao, R., M. M. Joglekar, and S. Inguva (2013) "A Phenomenological Degradation Model for Cyclic Aging of Lithium Ion Cell Materials," *Journal of The Electrochemical Society*, **160**(1), pp. A125–A137.

[58] Rahimian, S. K., S. C. Rayman, and R. E. White (2010) "Maximizing the Life of a Lithium-Ion Cell by Optimization of Charging Rates," *Journal of The Electrochemical Society*, **157**(12), pp. A1302–A1308.

[59] Pals, C. R. and J. Newman (1995) "Thermal Modeling of the Lithium/Polymer Battery: I . Discharge Behavior of a Single Cell," *Journal of The Electrochemical Society*, **142**(10), pp. 3274–3281.

[60] ——— (1995) "Thermal Modeling of the Lithium/Polymer Battery: II . Temperature Profiles in a Cell Stack," *Journal of The Electrochemical Society*, **142**(10), pp. 3282–3288.

[61] Srinivasan, V. and C. Y. Wang (2003) "Analysis of Electrochemical and Thermal Behavior of Li-Ion Cells," *Journal of The Electrochemical Society*, **150**(1), pp. A98–A106.

[62] Guo, M., G. Sikha, and R. E. White (2011) "Single-Particle Model for a Lithium-Ion Cell: Thermal Behavior," *Journal of The Electrochemical Society*, **158**(2), pp. A122–A132.

[63] Santhanagopalan, S., Q. Guo, P. Ramadass, and R. E. White (2006) "Review of models for predicting the cycling performance of lithium ion batteries," *Journal of Power Sources*, **156**(2), pp. 620 – 628.

[64] Shim, J., R. Kostecki, T. Richardson, X. Song, and K. Striebel (2002) "Electrochemical analysis for cycle performance and capacity fading of a lithium-ion battery cycled at elevated temperature," *Journal of Power Sources*, **112**(1), pp. 222 – 230.

Vita

Githin K. Prasad

Education:
The Pennsylvania State University, Ph.D. Mechanical Engineering, 2013.
The Pennsylvania State University, M.S. Mechanical Engineering, 2012.
National Institute of Technology Tiruchirappalli, B.Tech. Mechanical Engineering, 2008.

Work Experience:
Graduate Research Assistant, Sep 2009 - Sep 2013, The Pennsylvania State University
Graduate Teaching Assistant, Aug 2008 - May 2009, The Pennsylvania State University
Research Intern, June 2011 - Aug 2011, Robert Bosch Research and Technology Center, Palo Alto CA

Publications:

1. G.Prasad, C.Rahn,"Model Based Identification of Aging Parameters in Li-Ion Batteries", Journal of Power Sources.

2. G.Prasad, C.Rahn,"Reduced Order Impedance Models for Lithium Ion Batteries", Journal of Dynamic Systems and Control.

3. G.Prasad, C.Rahn, "Development of a First Principles Equivalent Circuit Model for a Lithium ion Battery ", ASME Dynamic Systems and Control Conference 2012, Ft.Lauderdale, FL.

4. Y.Shi, G.Prasad, Z.Shen, C.Rahn, "Discretization Methods for Battery Systems Modeling", American Control Conference 2011, San Francisco, CA.